Retrieval of Cirrus Microphysical Properties with a Suite of Algorithms for Airborne and Spaceborne Lidar, Radar, and Radiometer Data

YUYING ZHANG AND GERALD G. MACE

Department of Meteorology, University of Utah, Salt Lake City, Utah

(Manuscript received 24 June 2005, in final form 9 March 2006)

ABSTRACT

Algorithms are developed to convert data streams from multiple airborne and spaceborne remote sensors into layer-averaged cirrus bulk microphysical properties. Radiometers such as the Moderate-Resolution Imaging Spectroradiometer (MODIS) observe narrowband spectral radiances, and active remote sensors such as the lidar on the Cloud–Aerosol Lidar and Infrared Pathfinder Satellite Observation (CALIPSO) satellite and the millimeter radar on CloudSat will provide vertical profiles of attenuated optical backscatter and radar reflectivity. Equivalent airborne remote sensors are also routinely flown on the NASA WB-57F and ER-2 aircraft. Algorithms designed to retrieve cirrus microphysical properties from remote sensor data must be able to handle the natural variability of cirrus that can range from optically thick layers that cause lidar attenuation to tenuous layers that are not detected by the cloud radar. An approach that is adopted here is to develop an algorithm suite that has internal consistency in its formulation and assumptions. The algorithm suite is developed around a forward model of the observations and is inverted for layer-mean cloud properties using a variational technique. The theoretical uncertainty in the retrieved ice water path retrieval is 40%–50%, and the uncertainty in the layer-mean particle size retrieval ranges from 50% to 90%. Two case studies from the Cirrus Regional Study of Tropical Anvils and Cirrus Layers (CRYSTAL) Florida Area Cirrus Experiment (FACE) field campaign as well as ground-based cases from the Atmospheric Radiation Measurement Program (ARM) are used to show the efficacy and error characteristics of the algorithms.

1. Introduction

Cirrus clouds are a commonly occurring cloud type (Liou 1986; Dowling and Radke 1990; Wylie and Menzel 1999), having an annual global frequency of occurrence of about 30% (i.e., Wylie and Menzel 1989; Wylie et al. 1994; Rossow and Schiffer 1999). In tropical regions (from 30°S to 30°N) the coverage of cirrus is about 20% (Fu et al. 1990; Rossow and Schiffer 1999), and thin cirrus with optical thickness less than about 0.5 cover at least 5%–10% of the Tropics (Liao et al. 1995; Stubenrauch et al. 1999); approximately another 15% of the vast tropical region is covered by the subvisible cirrus with optical depth less than 0.03 (Wang et al. 1996).

Cirrus are a major component of the radiation budget of the earth–atmosphere system, where they significantly reduce the outgoing longwave radiation and often remain transmissive to solar energy (Stephens et al. 1990; Ackerman et al. 1988). General circulation models are, therefore, especially sensitive to the parameterization of cirrus (Del Genio et al. 1996). The relative magnitudes of cirrus spatial and temporal variability and their net effects depend primarily on cloud occurrence and also on the microphysical and radiative properties of the layers. Given the extreme variability of cirrus microphysical properties (Heymsfield et al. 2002), the effects of cirrus on the earth's radiation budget are not well documented from an observational perspective. This incomplete knowledge of cirrus cloud properties limits our ability to determine the magnitude of their net radiative impact (Stephens et al. 1990; Cess et al. 1996) on regional and global scales. This incomplete knowledge significantly hampers our ability to ensure that climate model predictions of climate change are physically reasonable. A global description of cirrus cloud properties that is consistent and well validated is, therefore, required.

Corresponding author address: Associate Professor Gerald G. Mace, 201 S. 1460 E. Rm. 819 (819 WBB), Department of Meteorology, University of Utah, Salt Lake City, UT 84112-0110.
E-mail: mace@met.utah.edu

In situ measurements provide the most direct information about cirrus microphysics, but the implementation cost and the often large measurement uncertainties make it difficult to use aircraft in situ data to develop globally applicable cloud statistics. Ground-based remote sensing, such as from the Atmospheric Radiation Measurement (ARM) Program (Ackerman and Stokes 2003), provides cloud information with high time and space resolution over long-term periods, but only at a few specific locations. Satellite observations conversely provide global datasets, although with less detail than either ground-based or aircraft in situ measurements. Operational algorithms are presently deriving cloud properties from several satellite-based radiometers (e.g., Platnick et al. 2001; Minnis et al. 1998; Rossow and Schiffer 1999). However, these algorithms are limited by an incomplete knowledge of the cloud being studied, such as layer height, physical thickness, and internal structure of clouds. The cloud properties retrieved using only radiometer observations are heavily dependent on a derived cloud temperature. An incorrect determination of the location of the hydrometeor layer in the vertical direction will produce errors in the retrievals (Miller et al. 2000). It is demonstrated by Cooper et al. (2003) that accurate cloud boundary information may increase the accuracy of the retrieved cirrus optical depth by a factor of 3. A strategy to document the global properties of clouds in general and cirrus in particular must rely heavily on each of these observational components, as we illustrate below.

With an ultimate goal of addressing the issues raised above using existing airborne datasets and future satellite measurements, we focus on the development of cirrus cloud property retrieval algorithms in this paper. These algorithms rely on narrowband radiance measurements from a passive radiometer, attenuated backscatter from an optical lidar, and radar reflectivity from a millimeter radar. Each of these measurements individually contains some unique information about the microphysical properties of an observed cirrus layer. Our goal is to exploit the synergy between these measurements.

The radiance measurements are provided by the Moderate-Resolution Imaging Spectroradiometer (MODIS; Salomonson 1990; Salomonson and Toll 1991) or its airborne equivalent the MODIS Airborne Simulator (MAS; King et al. 2004). These radiometers are cross-track multispectral-imaging instruments that, in the case of MODIS, presently fly on the National Aeronautics and Space Administration (NASA) *Terra* and *Aqua* satellites. The MAS has flown on many recent NASA field campaigns on the ER-2.

Radar reflectivity measurements will be obtained from the Cloud Profiling Radar (CPR) that will fly on CloudSat (Stephens et al. 2002) or its airborne equivalent the Airborne Cloud Radar (ACR; Li et al. 2004). Lidar backscatter will be obtained either from the lidar on the Cloud–Aerosol Lidar and Infrared Pathfinder Satellite Observation (CALIPSO) satellite or from the airborne equivalent the Cloud Profiling Lidar (CPL; McGill et al. 2004). The ACR, CPL, and MAS have flown on the NASA ER-2 in several recent field programs, and the CloudSat, CALIPSO, and *Aqua* satellites will fly in close formation so that their footprints will overlap spatially and will very nearly overlap temporally.

In this paper, section 2 describes the physical background of the observations, the simplifying assumptions we use to derive the forward-model equations, and the mathematical framework we use for inversion of the forward model. Particular attention is paid to developing forward models that can be inverted with high efficiency. The sensitivity of three potential algorithms to the input and empirical constants is also analyzed. In section 3, the algorithms are implemented using data collected during the Cirrus Regional Study of Tropical Anvils and Cirrus Layers (CRYSTAL) Florida Area Cirrus Experiment (FACE) (Jensen et al. 2004). Further evaluation of the current algorithms is performed using observations from MODIS on *Terra* combined with millimeter-wavelength cloud radar (MMCR) and micropulse lidar (MPL) data collected at the ARM Southern Great Plains (SGP) site.

2. Algorithm development

The combination of top-of-atmosphere radiances, radar reflectivity, and lidar backscatter is a powerful synergistic set of measurements capable of characterizing the properties of the majority of cirrus layers in the global upper troposphere. Our goal is to exploit this synergy to develop a suite of cloud property retrieval algorithms that will describe the bulk microphysical properties of cirrus layers.

While both CloudSat and CALIPSO are capable of profiling the vertical structure of cirrus, in this initial treatment we concentrate on layer-mean cloud properties. This approach is justified for practical and philosophical reasons. As we illustrate below with CRYSTAL FACE measurements, given the detection threshold of the radar and the tendency for the lidar to attenuate beyond optical depths of about 3, actual coincidence of simultaneously sampled vertical profiles will be relatively rare. Layers to which the radar will be sensitive will cause attenuation of the lidar beam, while portions of cirrus layers the lidar beam will penetrate

will often be undetected by the radar. Furthermore, focusing on layer-mean quantities allows us to bypass critical uncertainties and ultimately to derive information that is arguably more precise and more accurate. The cirrus layers we seek to examine with these algorithms are limited to layers with visible optical depths of less than about 5 to which MODIS IR radiances can provide unique information on layer emittance. Optically thicker layers can be treated with regression-based algorithms that rely on radar reflectivity (e.g., Liu and Illingworth 2000).

a. The observations

1) RADIOMETER DATA

We initially seek to convert measured radiance to cloud-layer emittance in one of the MODIS or MAS carbon dioxide (CO_2) spectral bands (channels 33, 34, or 35 of MODIS) (Wylie and Menzel 1989; Wylie et al. 1994). In the CO_2 bands, the absorbing gas is well mixed and the absorption is strong. We can, therefore, avoid having to characterize the lower atmospheric water vapor and surface temperature inherent to atmospheric window channels, except for, perhaps, in polar regions and over elevated terrain. Furthermore, because this is a thermal infrared radiance, cloud emissivity can be retrieved during nighttime as well as daytime. By assuming overcast cirrus observed in the field of view ($N = 1$), we have the following equation (Wylie and Menzel 1989; Wylie et al. 1994; Liou 2002):

$$\varepsilon = \frac{R(\lambda) - R_{\mathrm{clr}}(\lambda)}{B(\lambda, T_c) - R_{\mathrm{clr}}(\lambda)}, \tag{1}$$

where $R(\lambda)$ is the observed cloudy-sky radiance, $B(\lambda, T_c)$ is the Planck function at cloud-top temperature, and $R_{\mathrm{clr}}(\lambda)$ is an estimate of the clear-sky radiance based on the atmospheric state. Neglecting scattering and defining τ_a as the absorption optical depth, β_a as the layer-mean absorption coefficient, Δz as the cirrus layer thickness, Q_a as the absorption efficiency, and $n(D)$ as the particle size distribution, we can write $\varepsilon = 1 - \exp(\tau_a)$, $\tau_a = \beta_a \Delta z$, and

$$\beta_a = \int Q_a(D) D^2 n(D)\, dD, \tag{2}$$

relating the emissivity derived from the radiance measurement to the size-dependent absorption efficiency and second moment of the layer-mean particle size distribution.

2) LIDAR DATA

Lidars in the appropriate circumstances can provide vertical profiles of the volume backscatter coefficient and the volume extinction coefficient in optically transmissive clouds. The backscattered radiation detected by a lidar system is described by the lidar equation (Young 1995), where the lidar-signal voltage $V(r)$ produced by scattering at a range r from the lidar is

$$V(r) = (K/r^2)[\beta_m(r) + \beta_c(r)]T_m^2(0, r)T_c^2(r_b, r) + V_o, \tag{3}$$

where K is a system constant that includes output energy, receiver area, and so on and V_o is an offset voltage contributed by the sky background signal, detector dark current, and amplifier and digitizer offset voltages; $\beta_m(r)$ and $\beta_c(r)$ are the backscatter coefficients of molecular and cloud scatterers at range r, respectively; r_b and r_t are the ranges to cloud base and top, respectively;

$$T_m(0, r) = \exp\left[-\int_0^r \sigma_m(z)\, dz \right]$$

is the molecular transmittance from the lidar to range r; and

$$T_c(r_b, r) = \exp\left[-\int_0^r \eta(z)\sigma_c(z)\, dz \right]$$

is cloud transmittance from cloud base to range r within the cloud, where $\sigma_m(z)$ and $\sigma_c(z)$ are the molecular and cloud extinction coefficients, respectively. The factor $\eta(z)$ is an approximate representation of the effects of multiple scattering in the cloud, and $\sigma_c(z)$ can be written as

$$\sigma_c = \int Q_e(D) D^2 n\,(D)\, dD. \tag{4}$$

The transmittance of optically thin cirrus clouds can be determined using the lidar equation for profiles of backscatter and extinction from the elastically scattered lidar signals below and above the cloud. Backscatter lidar systems are typically calibrated using the known molecular (Rayleigh) backscatter determined by temperature, pressure, and chemical composition of the air. To determine cloud-layer transmissivity, we use lidar signals from two vertical layers above and below the cloud layer of interest. The satellite-measured lidar signal voltage in a region above the cloud can be expressed as (Mitrescu and Stephens 2002; Young 1995)

$$V(r) = (K/r^2)\beta_m(r)T_m^2(0, r) + V_o, \tag{5}$$

and in a region below the cloud the relationship becomes

$$V(r) = (K/r^2)\beta_m(r)T_m^2(0, r)T_c^2 + V_o. \tag{6}$$

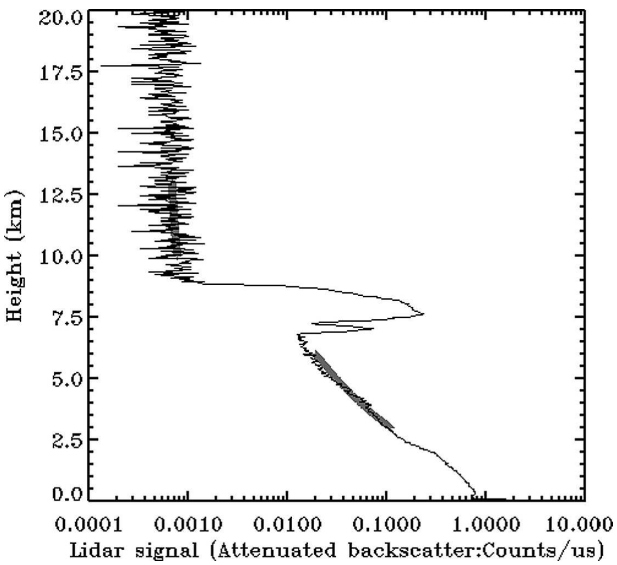

FIG. 1. Typical lidar backscattering signal for cloudy sky from ground-based instruments. Two independent layers of 3-km thickness are defined below (3–6 km) and above (10–13 km) the cloud layer. The fitted signals for the two layers are plotted as solid lines.

Aerosol is assumed to be absent in these two regions. Molecular backscatter and transmittance can be calculated from sounding data or model analysis output. Figure 1 is an example for the implementation of this method using ground-based lidar signals, with Eq. (5) for the layer below the cloud and Eq. (6) for the layer above the cloud. When the lidar signals can be fitted well in the two layers, cloud-layer transmissivity can be determined without additional knowledge of the relationship between backscatter and extinction. From the results of a simulated case (Mitrescu and Stephens 2002), error in the estimated transmittance has been shown to be within 20%.

3) RADAR DATA

Assuming the Rayleigh approximation is valid (Schneider and Stephens 1995) and neglecting for the moment differences in the refractive indexes of ice and water, Z_e is identical to the radar reflectivity factor

$$Z = \int_0^\infty N(D)D^6\, dD, \tag{7}$$

where D is the diameter of spherical particles. The standard radar observable is the water-equivalent radar reflectivity factor Z_e from the radar equation. If the targets are ice particles, the radar reflectivity factor of ice Z_i is related to Z_e by $Z_e = Z_i(K_i^2/K_w^2)$, where Z_i is given by Eq. (10). Here, K_w depends on the complex index of refraction of liquid (Doviak and Zrnic 1993), and K_i corresponds to that of ice (Warren 1984).

TABLE 1. The suite of algorithms proposed for characterizing the layer-averaged microphysical properties of cirrus with A-Train measurements. Rows of the table show with an X which observations are used to construct a set of forward-model equations using the assumed size distribution functional form in the right-hand column.

Observations			
Radar	Lidar	Radiometer	
Z	$T(\beta_{\text{ext}})$	$\varepsilon(\beta_{\text{abs}})$	Assumption
X	X		$n(L) = n_e \exp(-\lambda_e L)$
X		X	
	X	X	

b. Development of the forward-model equations

We exploit the fundamental differences in the manner in which the electromagnetic radiation used by the three remote sensors interacts with a cirrus layer. Unlike the optical scattering and infrared absorption cross sections, the radar backscatter cross section depends on the sixth moment of the particle size distribution. Also, because the scattering cross section at the microwave frequency of the radar is relatively very small in comparison with the scattering cross section at optical wavelengths, the radar pulse can penetrate optically thick clouds (absorption by ice particles is negligible at the radar and lidar frequencies). Although both the infrared emissivity and the optical extinction are sensitive to the second moment of the particle size distribution as shown in Eqs. (2) and (4), their absorption and scattering efficiencies have different dependencies on particle size (this effect is illustrated in more detail below).

Table 1 is a schematic of the algorithm suite that takes advantage of these unique aspects of the three measurements. Each row of the table represents a specific algorithm for retrieving layer-mean cloud properties where the algorithm forward models are based on a common set of simplifying assumptions, as described below. The radar–lidar algorithm (row 1 of Table 1) is hereinafter referred to as the ZS algorithm, the radar–radiometer algorithm (row 2 of Table 1) is referred to as the ZR algorithm, and the radiometer–lidar algorithm (row 3 of Table 1) is referred to as the RS algorithm.

1) ASSUMPTIONS USED IN CONSTRUCTION OF THE FORWARD-MODEL EQUATIONS

To retrieve cloud properties, the layer-mean ice crystal size spectrum is assumed following Heymsfield

(2003) in the form of a two-parameter exponential function $n(L) = N_e \exp(-\lambda_e L)$ (note that henceforward we use L to denote the particle maximum dimension whereas D is used to represent spherical equivalent diameters). The number per unit length per unit volume of particles is N_e, and the logarithmic slope of the size spectrum is λ_e and has units of inverse length. Although particle spectra with bimodal tendencies are common, Mace et al. (2002) showed that single-mode functions are reasonably capable of capturing the essential characteristics of cirrus particle spectra within observational uncertainty for most cirrus when the radar reflectivity factor is less than about -5 dBZ_e and temperatures are colder than about -20°C. This is especially the case when considering layer-mean quantities.

Because ice crystals are not solid spheres of diameter L, the forward model must include a set of empirical expressions that relate the maximum dimension of an ice crystal with the particle cross-sectional area $[A(L)]$, radar backscatter cross section, and particle mass $[m(L)]$. It is a conventional approach to express these relations in a power-law form in which the coefficients depend on crystal habit (Mitchell 1996; Aydin and Walsh 1999; Heymsfield and Iaquinta 2000; Heymsfield et al. 2002):

$$A(L) = a_A L^{b_A},$$

$$m(L) = a_m L^{b_m}, \qquad \text{and}$$

$$Z = \int_0^\infty a_z L^{6+b_z} n(L)\, dL,$$

where (a_A, a_m, and a_z) and (b_A, b_m, and b_z) are coefficients of the power-law relationships. For different ice crystal habits, the coefficients vary significantly (Heymsfield et al. 2004; Mitchell 1996; Mace et al. 2002), and algorithms that make assumptions regarding any of these or other similar parametric relationships are sensitive to uncertainties associated with them. Using coefficients found in various publications based primarily on in situ data collected in the northern midlatitudes (e.g., Mitchell 1996; Heymsfield and Iaquinta 2000; Heymsfield et al. 2002), we have developed lookup tables that assume a crystal habit progression from pristine columns at cold temperatures to aggregates of various habits at warmer temperatures.

2) Development of the forward-model equations

The infrared absorption coefficient is expressed in Eq. (2) and is estimated from the layer emissivity. Data for the absorption efficiency Q_a as a function of ice particle maximum dimension L in the CO_2 channel (13–14 μm) is provided by Yang et al. (2004) and is based on a composite of T_matrix, Geometric Optics Method, and Mie theory results. We fit a function of the form

$$Q_a(L) = g + \sum_{i=1}^{i=3} a_i (L - b_i) \exp[-c_i (L - d_i)]$$

to the calculated Q_a (Fig. 2). The coefficients of this function are listed in Table 2.

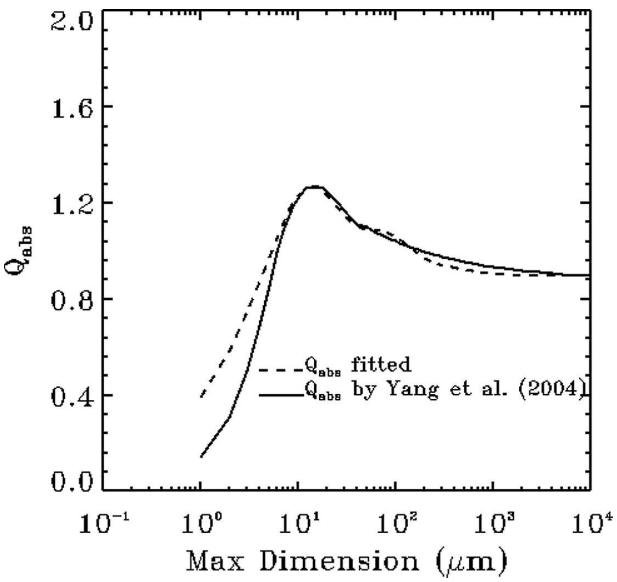

FIG. 2. The Q_{abs} as a function of the maximum dimension (μm) of ice crystals.

The visible extinction coefficient at lidar wavelengths is expressed in Eq. (4). It is estimated from the cloud transmissivity $[T = \exp(-\tau)]$, and Q_{ext} is assumed to be a constant 2 because the particles are on the order of tens to hundreds of micrometers, whereas the lidar wavelengths are in the 0.5-μm range.

Radar reflectivity factor Z_e is expressed as

$$Z_e = a_z \int_0^\infty n(L) L^{6+b_z}\, dL. \tag{8}$$

TABLE 2. Coefficients for expressing Q_a for the CO_2 between 13.549 and 14.075 μm as a function of the maximum dimension of ice crystals (μm).

i	g_i	a_i	b_i	c_i	d_i
1	0.9	0.029	3.5	0.12	15.0
2		0.0085	10.0	0.02	15.0
3		0.000 25	40.0	0.0046	150.0

TABLE 3. Sensitivity analysis of retrieved properties to the observations. Here, Z refers to radar reflectivity factor, R refers to emissivity derived from radiometer data, S refers to lidar-retrieved transmissivity, minus signs refer to a decrease, plus signs refer to an increase, "1" refers to 10%, and "2" refers to 20%.

ZR		ZS		RS	
ΔIWC/IWC	$\Delta L_{\text{mass}}/L_{\text{mass}}$	ΔIWC/IWC	$\Delta L_{\text{mass}}/L_{\text{mass}}$	ΔIWC/IWC	$\Delta L_{\text{mass}}/L_{\text{mass}}$
0.15(Z+1)	0.29(Z+1)	0.15(Z+1)	0.35(Z+1)	0.36(S−1)	0.62(S−1)
−0.13(Z−1)	−0.23(Z−1)	−0.13(Z−1)	−0.26(Z−1)	−0.71(S+1)	−0.90(S+1)
0.33(Z+2)	0.67(Z+2)	0.33(Z−2)	0.82(Z+2)	0.55(S−2)	0.90(S−2)
−0.25(Z−2)	−0.41(Z−2)	−0.25(Z+2)	−0.45(Z−2)	−0.90(S+2)	−0.99(S+2)
−0.11(R−1)	0.07(R−1)	0.08(S−1)	−0.04(S−1)	0.19(R−1)	0.60(R−1)
0.11(R+1)	−0.06(R+1)	−0.07(S+1)	0.05(S+1)	−0.59(R+1)	−0.85(R+1)
−0.20(R−2)	0.15(R−2)	0.16(S−2)	−0.09(S−2)	0.20(R−2)	0.91(R−2)
0.23(R+2)	−0.12(R+2)	−0.14(S+2)	0.09(S+2)	−0.77(R+2)	−0.96(R+2)

The basic microphysical properties of cirrus clouds that we derive from the observations are ice water content (IWC) and mass-mean length L_{mass}:

$$\text{IWC} = \int_0^\infty m(L)n(L)\,dL \quad \text{and} \tag{9}$$

$$L_{\text{mass}} = \int_0^\infty Lm(L)n(L)\,dL \Big/ \int_0^\infty m(L)n(L)\,dL. \tag{10}$$

Equations (2), (4), and (8), assuming an exponential size distribution and using the power-law relations listed earlier, become

$$\beta_a = \frac{ga_AN_e}{\lambda_e^{1+b_A}}\Gamma(1+b_A) + \sum_{i=1}^{i=3}\frac{a_ia_AN_e\exp(c_id_i)}{(c_i+\lambda_e)^{2+b_A}} \times [\Gamma(2+b_A) - b_i(c_i+\lambda_e)\Gamma(1+b_A)], \tag{11a}$$

$$\beta_{\text{ext}} = \frac{2a_AN_e}{\lambda_e^{1+b_A}}\Gamma(1+b_A), \quad \text{and} \tag{11b}$$

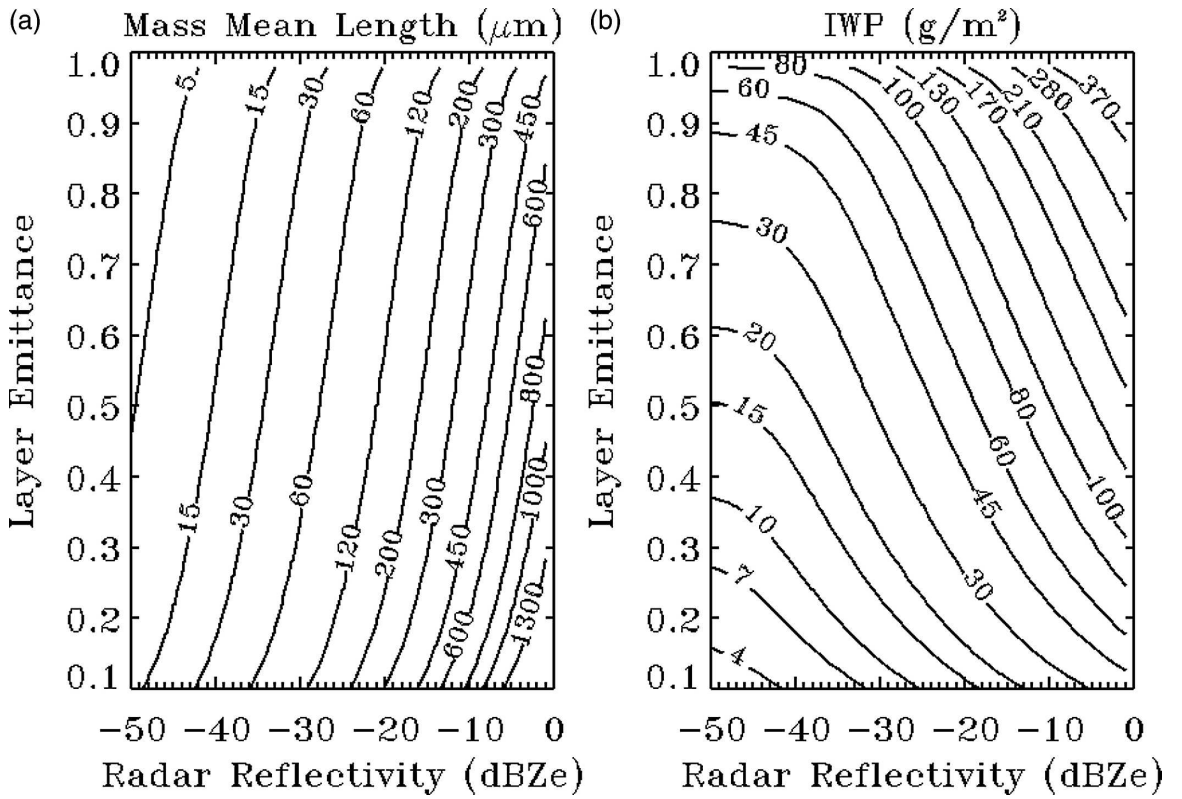

FIG. 3. Sensitivity of the ZR algorithm for typical values of layer emittance and radar reflectivity. The assumed cloud depth is 2 km: (a) mass-mean length (μm) and (b) ice water path (g m^{-2}).

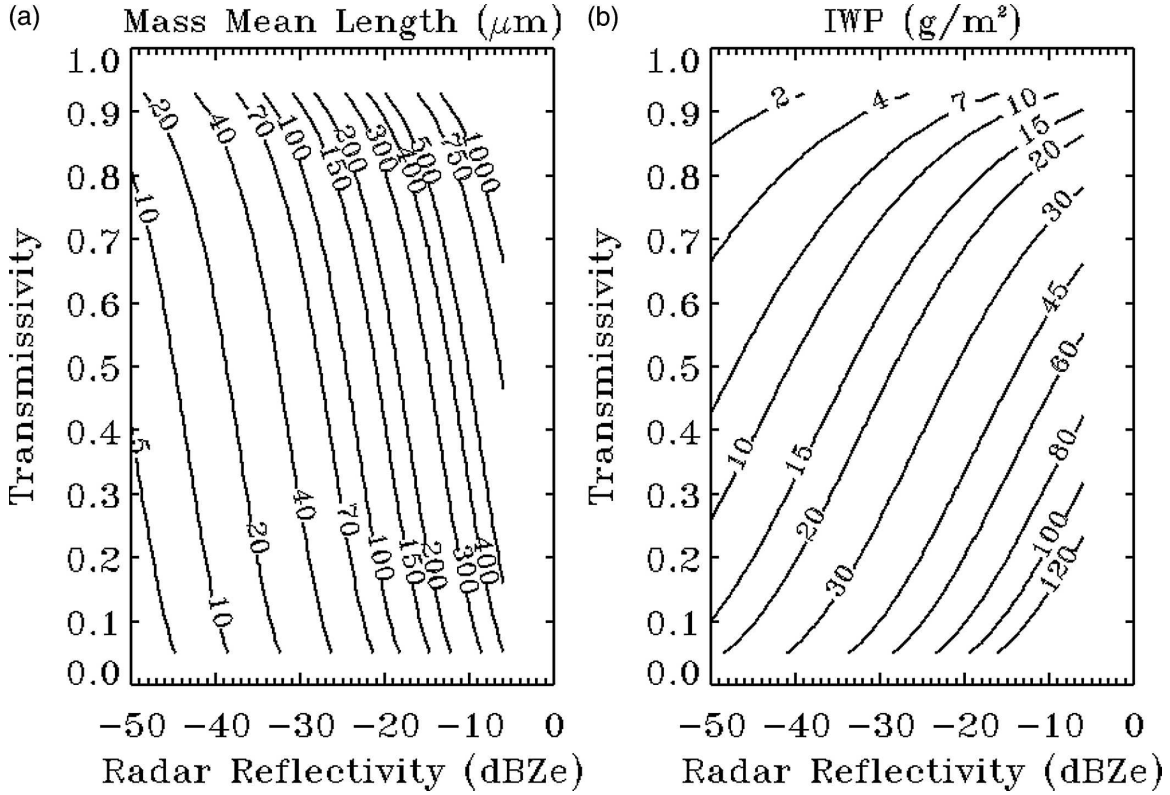

FIG. 4. Sensitivity of the ZS algorithm for typical values of layer transmittance and radar reflectivity. The assumed cloud depth is 2 km: (a) mass-mean length (μm) and (b) ice water path (g m^{-2}).

$$Z_e = \frac{a_z N_e}{\lambda_e^{7+b_z}} \Gamma(7 + b_z), \tag{11c}$$

where Γ is the gamma function [$\Gamma(z) = \int_0^\infty t^{z-1} e^{-t}\, dt$]. Therefore, the characteristics of the assumed particle size distribution can be inferred from observations of Z_e, β_a, and β_{ext} averaged over the cirrus layer. Any two observations can then be combined to retrieve the ice crystal size distribution. Once λ_e and N_e are known, other parameters of interest can be derived. For example, IWC and mass-mean length L_{mass} can be written as

$$\text{IWC} = \frac{a_m N_e}{\lambda^{1+b_m}} \Gamma(1 + b_m) \quad \text{and} \tag{12}$$

$$L_{\text{mass}} = (1 + b_m)/\lambda_e. \tag{13}$$

The forward models of the algorithms listed in the three rows of Table 1 can be constructed using combinations of expressions in Eq. (11). Our models of the observations depend explicitly on six empirically derived parameters (a_z, b_z, a_m, b_m, a_A, and b_A), whereas the microphysical parameters of interest (IWC and L_{mass}) depend only on the empirical relationship between particle size and particle mass.

To frame the algorithms so that a formal error analysis is possible, it is most straightforward to include a_m and b_m explicitly in the forward-model equations. Therefore, using the expressions for IWC and L_{mass}, N_e and λ_e are eliminated in Eq. (11), with the result that

$$\beta_a = \frac{g a_A \Gamma(1 + b_A)\text{IWC}}{a_m \Gamma(1 + b_m)} \left(\frac{L_{\text{mass}}}{1 + b_m}\right)^{b_A - b_m} + \sum_{i=1}^{i=3} \frac{a_i a_A \exp(c_i d_i)}{[c_i + (1 + b_m)/L_{\text{mass}}]^{2+b_A}} \frac{\text{IWC}}{a_m \Gamma(1 + b_m)} \left(\frac{1 + b_m}{L_{\text{mass}}}\right)^{1+b_m}$$

$$\times \left[\Gamma(2 + b_A) - b_i \left(c_i + \frac{1 + b_m}{L_{\text{mass}}}\right) \Gamma(1 + b_A)\right], \tag{14a}$$

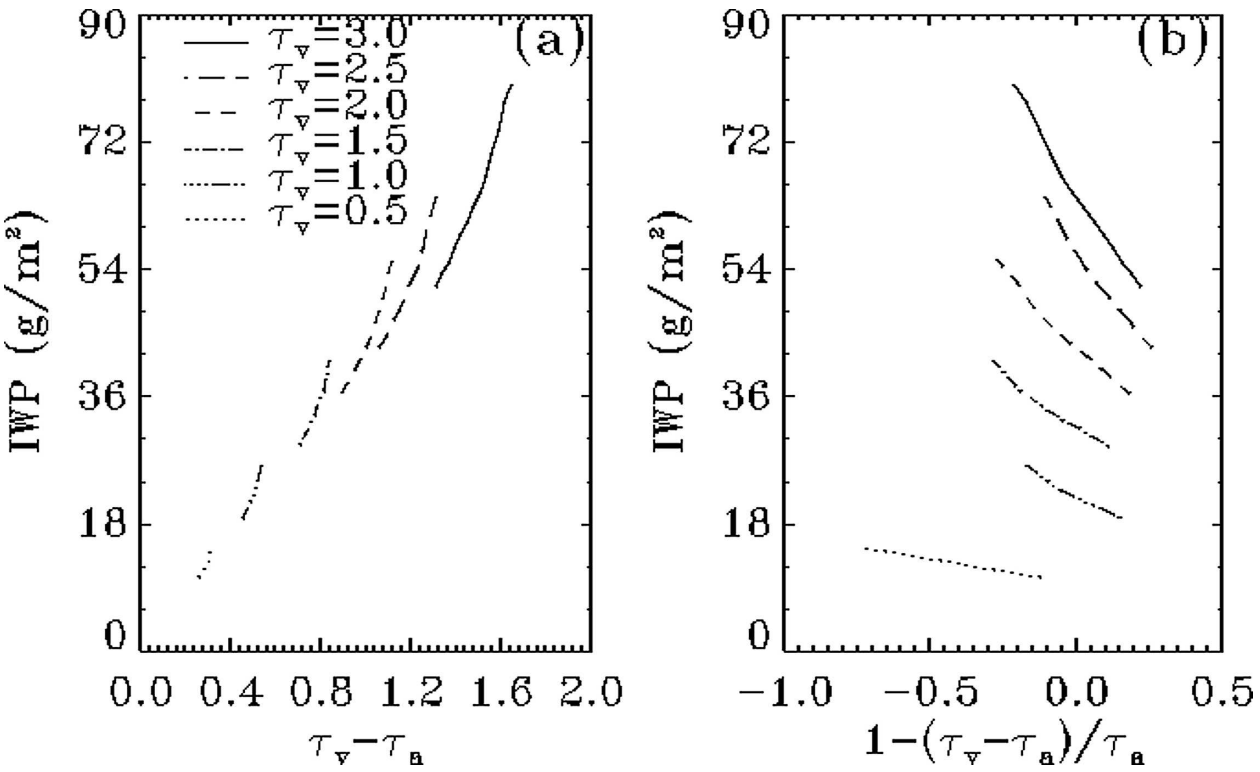

FIG. 5. Retrieved IWP (assuming 2-km-thick cirrus cloud) as a function of the (a) difference and (b) fractional difference between the visible (τ_v) and infrared (τ_a) optical thicknesses.

$$\beta_{\text{ext}} = \frac{2a_A\Gamma(1+b_A)\text{IWC}}{a_m\Gamma(1+b_m)}\left(\frac{L_{\text{mass}}}{1+b_m}\right)^{b_A-b_m}, \quad \text{and} \tag{14b}$$

$$Z_e = \frac{a_z\Gamma(7+b_z)\text{IWC}}{a_m\Gamma(1+b_m)}\left(\frac{L_{\text{mass}}}{1+b_m}\right)^{6+b_z-b_m}. \tag{14c}$$

3) FORWARD-MODEL INVERSION USING OPTIMAL ESTIMATION

The forward models represented by Eq. (14) are expressed in terms of two unknowns (L_{mass} and IWC), any combination of two observations (Z_e and β_{ext}, Z_e and β_a, or β_a and β_{ext}), and six empirically derived parameters that are coefficients of power-law relationships. The expressions representing particle area and particle mass in terms of particle size are functions of particle habit and, therefore, may vary significantly from case to case and result in uncertainty in the retrieved L_{mass} and IWC. Observational uncertainty must also be accounted for.

We invert the set of forward-model equations [$\mathbf{y} = F(\mathbf{x})$] for the state vector $\mathbf{x}$ = (IWC, L_{mass}) using the

TABLE 4. Sensitivity analysis of retrieved properties to empirical constants of the power-law expressions.

		ΔIWC/IWC			$\Delta L_{\text{mass}}/L_{\text{mass}}$		
		ZR	ZS	RS	ZR	ZS	RS
$\Delta a_m/a_m$	0.1	0.1	0.1	0.09	-3.50×10^{-7}	0	−0.02
	−0.1	−0.1	−0.1	−0.09	4.67×10^{-7}	0	0.02
$\Delta b_m/b_m$	0.1	−1.2	−1.25	−0.59	0.07	0.06	0.1
	−0.1	0.50	0.55	0.37	−0.07	−0.06	−0.09
$\Delta a_z/a_z$	0.1	−0.03	−0.03	0	−0.05	−0.05	0
	−0.1	0.02	0.02	0	0.04	0.05	0
$\Delta b_z/b_z$	0.1	−0.13	−0.22	0	−0.46	−0.53	0
	−0.1	0.14	0.22	0	0.37	0.41	0
$\Delta a_A/a_A$	0.1	−0.08	−0.08	−0.1	0.05	0.05	0.02
	−0.1	0.07	0.07	0.08	−0.04	−0.05	−0.01
$\Delta b_A/b_A$	0.1	0.35	0.37	0.3	−0.47	−0.53	−0.09
	−0.1	−0.6	−0.69	−0.42	0.37	0.39	0.1

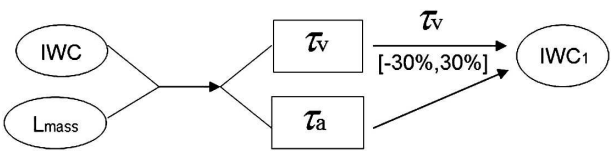

FIG. 6. The method used to calculate the sensitivity of the retrievals to the uncertainty in input data. The initial IWC (varies in the typical range) and L_{mass} (fixed at 0.02 cm) are combined to calculate the corresponding τ_v and τ_a, τ_v changes by a fraction that ranges from −30% to 30%, and the changed τ_v is combined with initial τ_a to derive new IWC_1.

optimal estimation approach (Rodgers 2000; Benedetti et al. 2003). Rodgers (2000) shows that the solution can be found by calculating the a posteriori probability density function of **x** given **y**, $P(\mathbf{x}|\mathbf{y})$, in a Bayesian sense in which a state vector ($\hat{\mathbf{x}}$) of maximum likelihood with uncertainty is estimated. The solution requires finding where the gradient of $P(\mathbf{x}|\mathbf{y})$ in terms of **x** is zero. The gradient minimum can be numerically estimated using a Gauss–Newton iterative approach [i.e., Eq. (5.8) of Rodgers 2000]:

$$\mathbf{x}_{i+1} = \mathbf{x}_i + (\mathbf{S}_a^{-1} + \mathbf{K}_{x,i}^{\mathrm{T}}\mathbf{S}_{y,i}^{-1}\mathbf{K}_i)^{-1} \times \{\mathbf{K}_{x,i}^{\mathrm{T}}\mathbf{S}_{y,i}^{-1}[\mathbf{y} - F(\mathbf{x}_i)] - \mathbf{S}_a^{-1}(\mathbf{x}_i - \mathbf{x}_a)\}. \quad (15)$$

In Eq. (15), $\mathbf{K}_{x,i}$ is the ith estimate of the sensitivity of the forward model to the unknown quantities $\mathbf{K}_x$ and $\mathbf{S}_a$ is the covariance matrix of the a priori data $\mathbf{x}_a$. One of the distinct advantages of solving the forward-model equations using a variational approach is the ability to estimate rigorously the algorithm error and to be able to determine what input parameters and assumptions contribute most significantly to the error.

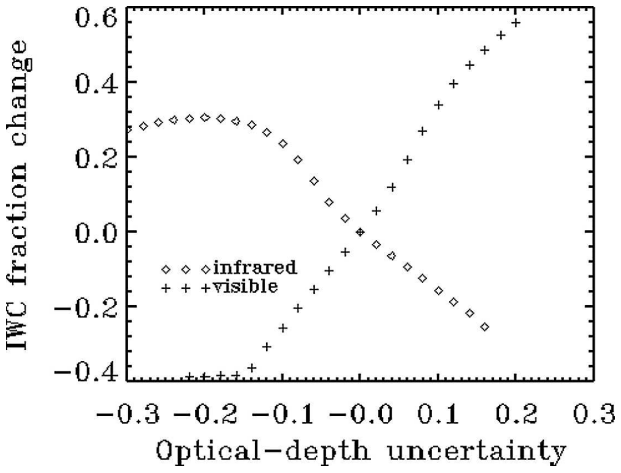

FIG. 7. The IWC fractional change is expressed as (IWC_1 − IWC)/IWC. The x axis is the uncertainties of optical thicknesses used to retrieve IWC1.

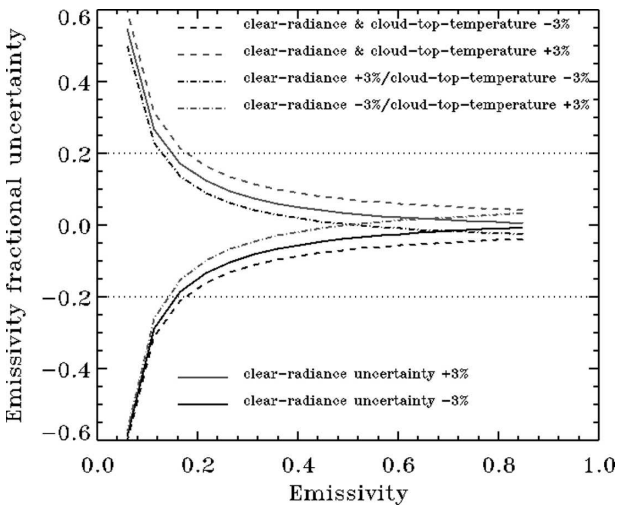

FIG. 8. Assuming a 3% possible uncertainty for the cloud-top temperature and clear-sky radiance, the fractional uncertainty in emissivity is shown for different emissivities.

c. Sensitivity study

The sensitivity of retrieved cloud microphysical properties for typical values of the observations is shown in Table 3 and Figs. 3, 4 and 5. Figure 3 is calculated from the ZR algorithm that combines Eqs. (14a) and (14c). Figure 4 is calculated from the ZS algorithm in which Eqs. (14b) and (14c) are used. The retrieved parameters depend to a nearly equal degree on the input

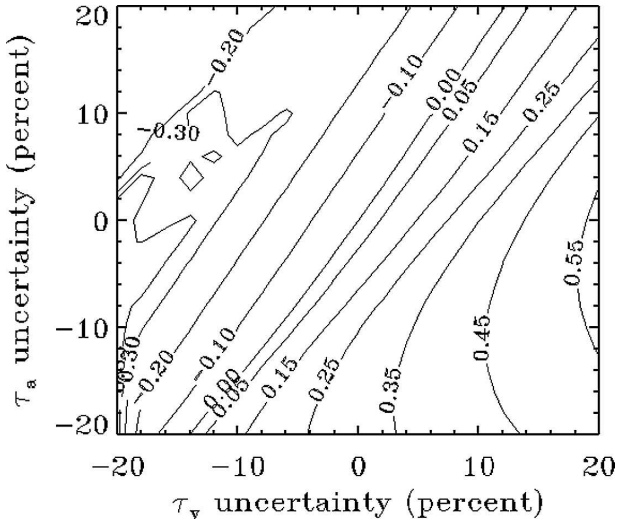

FIG. 9. The retrieval uncertainty of RS-derived IWC (fractional amount) to the combined input errors (expressed in percent).

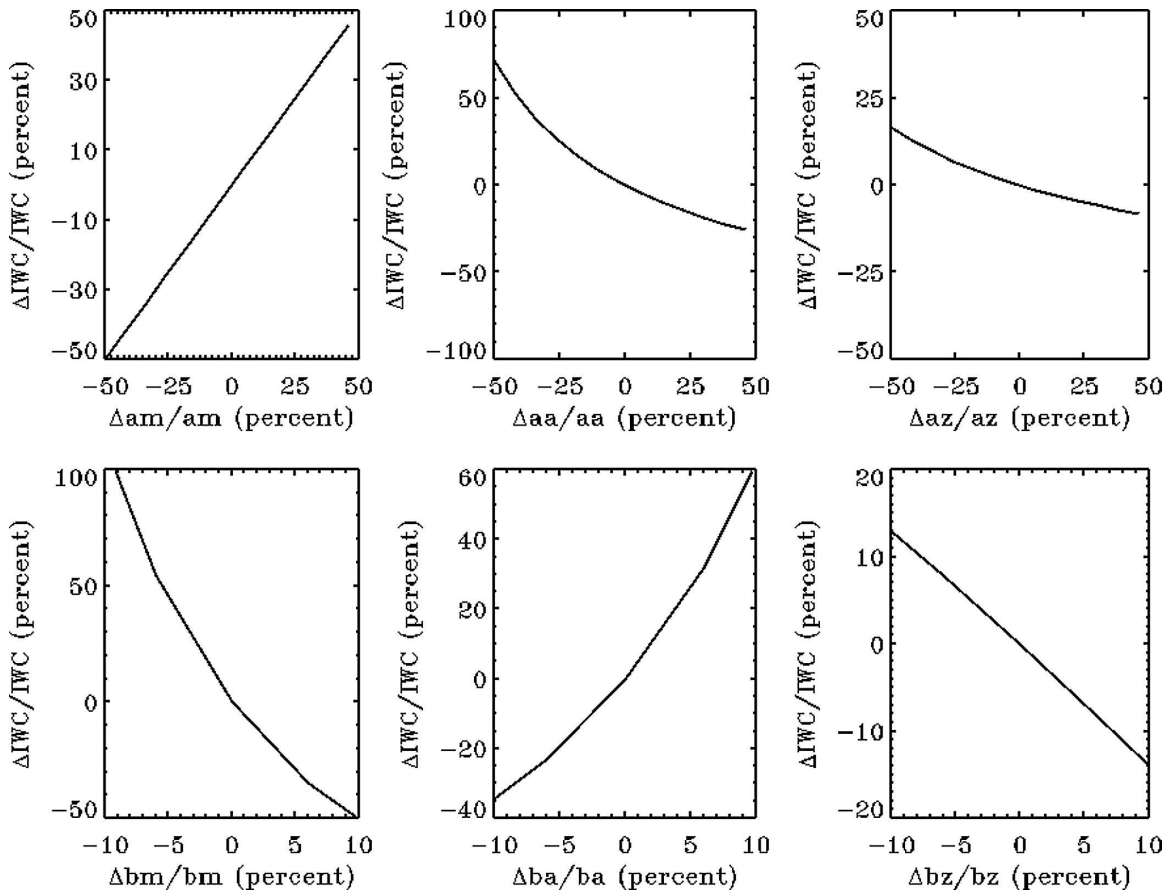

FIG. 10. The sensitivity of IWC to the empirical constants for the ZR algorithm. Here, a_a and b_a are used in place of a_A and b_A in the x-axis labels in the middle column.

parameters, and the retrieval results tend to remain within the ranges typical of cirrus (Dowling and Radke 1990; Mace et al. 2001). For a given radar reflectivity, the water content increases and the mass-mean length decreases for increasing emittance, and the water content decreases and the mass-mean length increases for increasing transmittance. Holding the emittance or the transmittance constant, all parameters increase with increasing radar reflectivity. Particle size is more sensitive to radar reflectivity than to emissivity, which is expected, because radar reflectivity is related to a high moment (greater than 4 and less than 5) of the size distribution, and both transmittance and emissivity are related to approximately the second moment of the size distribution. The two figures also suggest that the ice water path (IWP) is most sensitive to observational errors at larger values of radar reflectivity and emittance and smaller values of transmittance, whereas particle size is most sensitive to errors at the larger values of radar reflectivity and transmittance and smaller values of emittance.

The algorithm combining infrared emissivity and lidar-derived transmittance is similar in principal to the lidar and infrared radiometer (LIRAD) algorithm pioneered by M. Platt (Platt and Dilley 1981). In this algorithm, both measurements are related to the second moment of the crystal size distribution. Therefore, the measurements can be expected to vary more or less systematically with one another. The information to solve the system of equations for IWC and L_{mass} comes from the different dependencies of infrared Q_a and visible Q_e on particle size. Small changes in one observation relative to the other will cause a large change in the retrieved values. We can expect this algorithm to be the most unstable algorithm of the three considered, as shown in Table 4.

Because a large portion of the cirrus in the Tropics is of small optical depth (<1) and some unknown but substantial fraction of this cirrus is below the sensitivity threshold of the CPR and other airborne cloud radars (Comstock et al. 2002), we anticipate that the RS algorithm will be germane to many cirrus cases. The sensi-

TABLE 5. Theoretical errors in the retrieved IWP and L_{mass} resulting from expected uncorrelated observational errors and uncorrelated uncertainties in the empirical relationships as described in the text.

	IWP	L_{mass}
ZR	40%	50%
ZS	40%	50%
RS	50%	90%

tivity of the RS algorithm is depicted in Figs. 5–9. Assuming a cloud-layer thickness of 2 km, Fig. 5 shows the IWP changes as a function of the difference between the visible (τ_v) and infrared (τ_a) optical thicknesses. IWP increases systematically as the visible optical depth increases. The method in Fig. 6 is used to test the sensitivity of the layer-mean IWC to the uncertainty of τ_v and the sensitivity of IWC to the uncertainty of τ_a is tested with a similar approach. The initial IWC and L_{mass} (fixed at 0.02 cm) are converted to τ_v and τ_a, τ_v changes from −30% to +30%, and the changed τ_v is combined with initial τ_a to derive a perturbed IWC. The results are shown in Fig. 7. The IWC fractional change is not a function of the absolute value of τ_v (or τ_a) and only depends on fractional uncertainty of τ_v (or τ_a). Absolute uncertainty in IWC increases at a rate that is about 2 times as fast as the uncertainty in the input optical depths, although the trend in the sign of the error is opposite.

Because both the visible (τ_v) and infrared (τ_a) optical thicknesses would tend to have uncertainties, we consider the IWC uncertainty with simultaneous input errors. The method we use to obtain visible optical thickness (τ_v) has an uncertainty on the order of 20%, and this error would be largest for very small optical depths (<0.1) and for layers that very nearly attenuate the lidar signal. In our approach to estimating the infrared emissivity ε, we assume a 3% uncertainty in the determination of cloud-top temperature or about 6 K in the upper troposphere. We assume a similar error in the calculated clear-sky radiance, although this value will depend on the quality of the input atmospheric sounding. Because the MODIS observation has an uncertainty below 0.5% at the CO_2 channels, only the uncertainty of the clear-sky radiance calculated from the radiative transfer model is considered. With these assumptions we find the uncertainty in ε (Fig. 8) is less than 20% when ε is larger than 0.1. The corresponding IWC fractional change, allowing for uncertainty in both input parameters, is shown in Fig. 9. When uncertainties in τ_v and τ_a are large, which is especially true for small optical depths, the IWC is very sensitive to these uncertainties and the retrievals may not be reliable. We

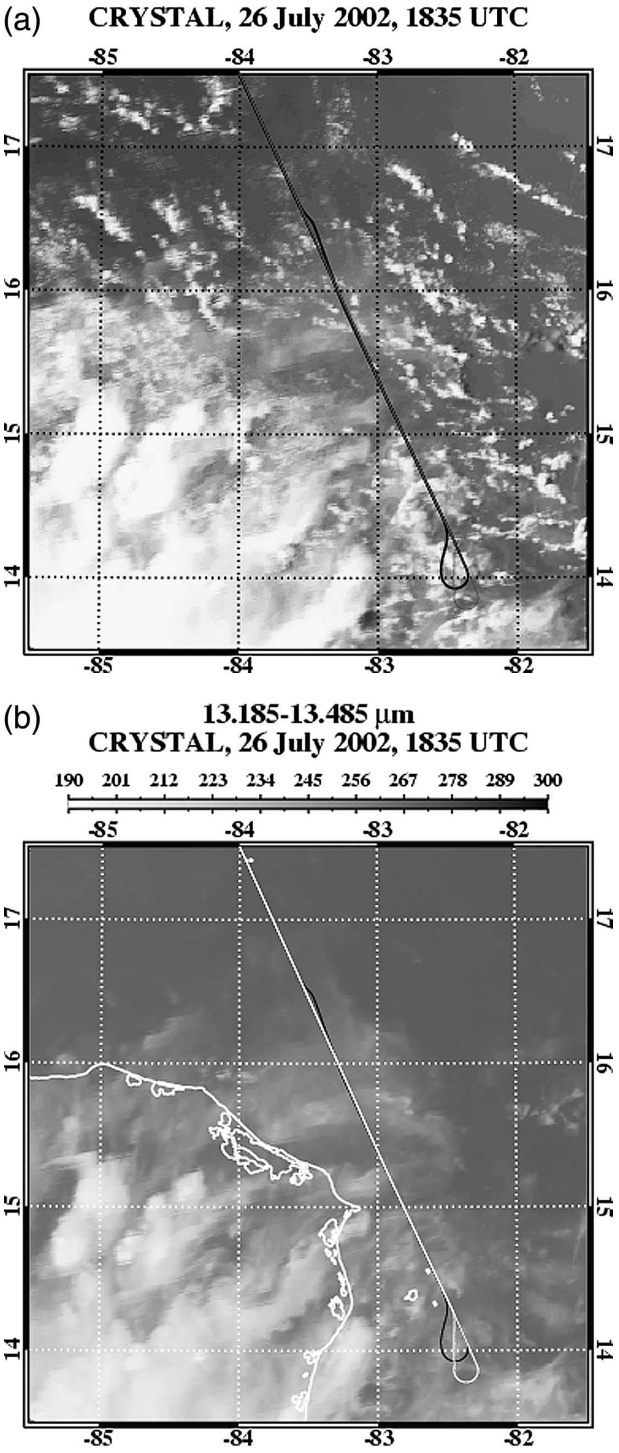

FIG. 11. (a) The visible-channel observations from MODIS on *Aqua* with the ER-2 aircraft flight track in gray and WB-57F aircraft flight track in black. (b) The CO_2-channel observations from MODIS on *Aqua* with the ER-2 aircraft flight track in white and WB-57F aircraft flight track in black.

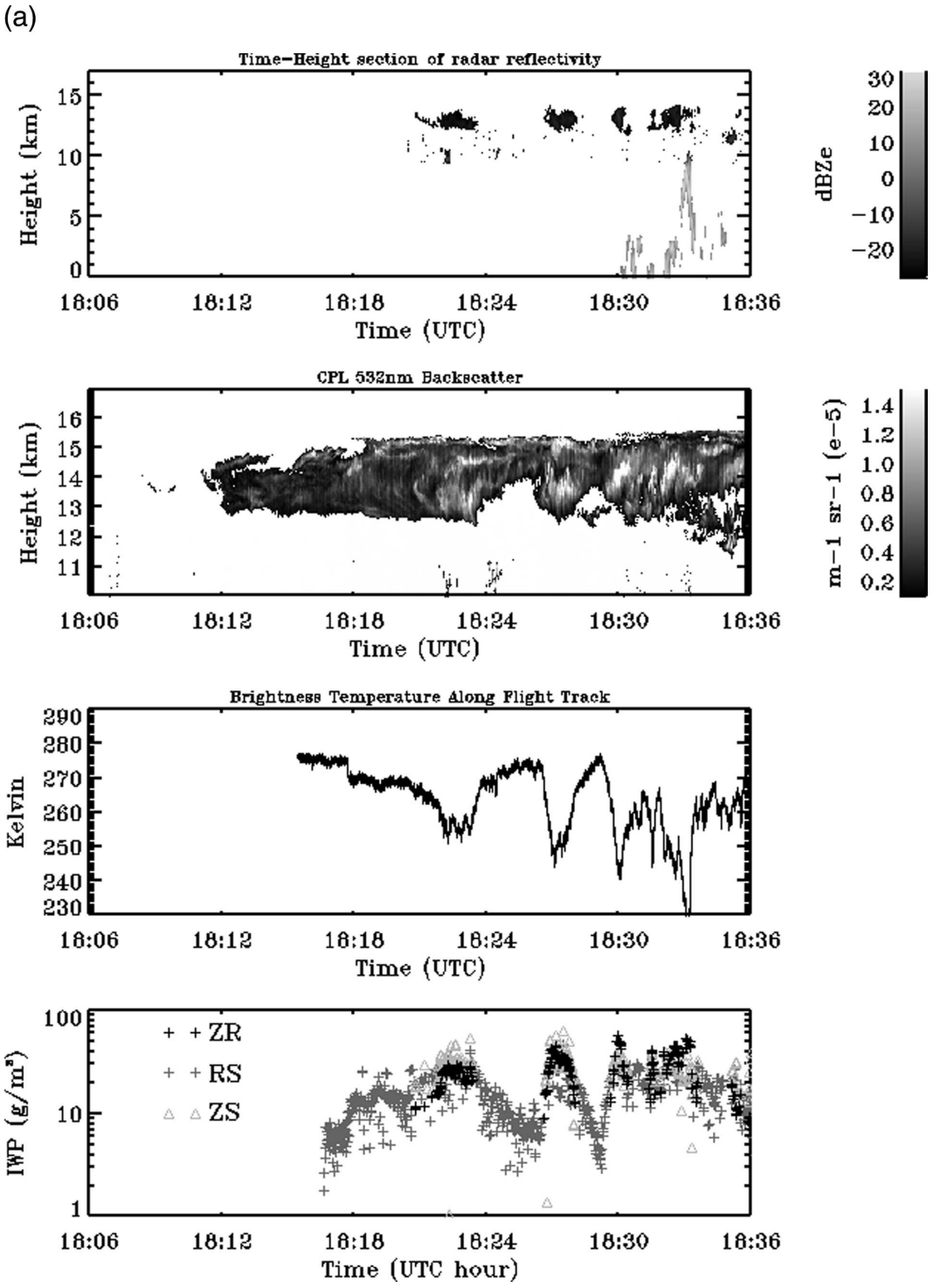

FIG. 12. (a) Southbound leg and (b) northbound leg for CRS, CPL, T_b, and retrieved IWC on 26 Jul 2002.

do note a tendency for the errors to compensate one another when the errors are of opposite sign, although we do not expect correlation in the uncertainty of the errors in the input values.

As shown in Table 4, the retrieved properties are sensitive to the empirical constants assumed in all of the algorithms. The compilation by Mitchell (1996) shows, for instance, that the exponent in the mass dimensional

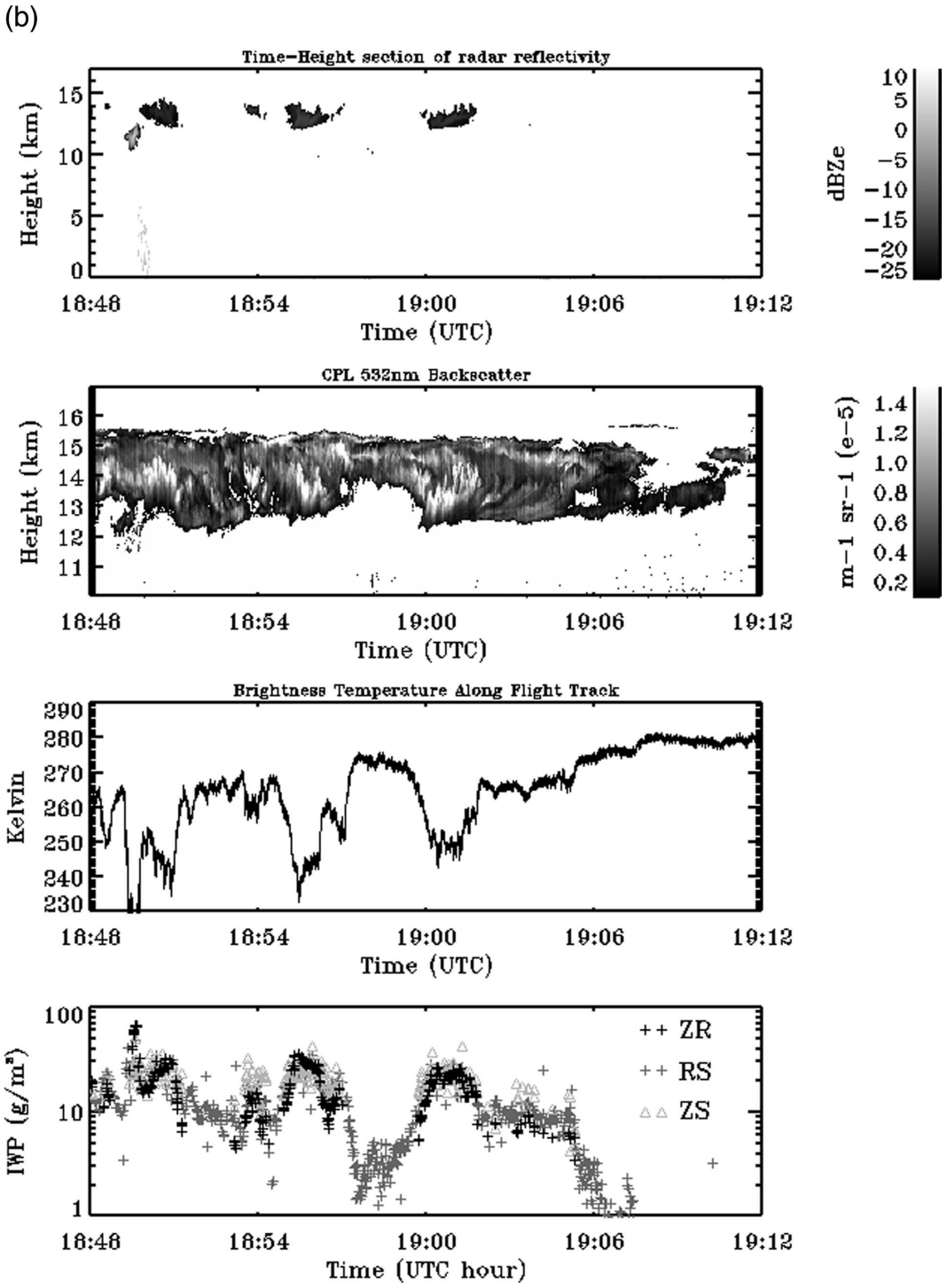

FIG. 12. (*Continued*)

power law varies from about 1.9 for large columns and side-plane aggregates to about 3 for small spheroidal crystals. An average value is likely to be on the order of about 2.25 (bullet rosettes). In the ZR algorithm (Fig. 10), when a_m decreases and increases 50%, IWC changes linearly, but the change is nonlinear with a_A and a_z. The retrieved IWC is especially sensitive to the specified values of b_m, b_A, and b_z. Table 4 shows the

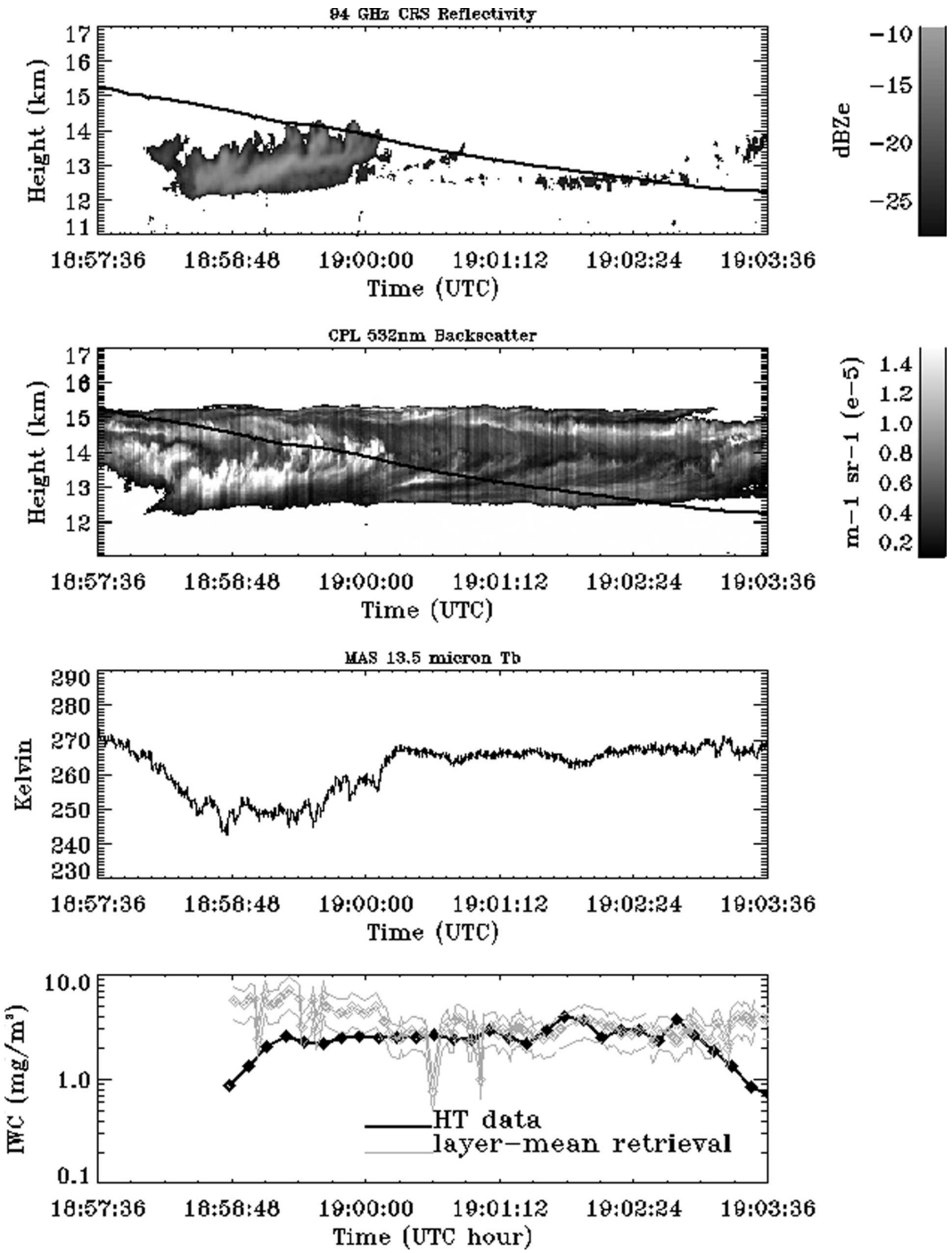

FIG. 13. WB-57F aircraft flight track plotted together with ER-2 radar and lidar observations, and retrieved layer-mean IWC compared with in situ data [Harvard (HT) data provided by E. Weinstock, Harvard University].

sensitivities of the retrieval algorithm results to power-law empirical constants for all three algorithms. This analysis shows that large uncertainties in the retrievals arise because of small uncertainties in the empirical constants. For example, the change of IWC for the ZR and ZS algorithms can exceed a factor of 2 with a 10% error in b_m. The change of IWC is somewhat smaller with the uncertainties in b_z and b_A. These results highlight the fact that global retrievals of ice cloud microphysical properties require a library of these coeffi-

cients with reasonably defined statistical uncertainties; such a library at this point does not exist. Such a library would be based on in situ aircraft data, in which ice crystal area, size, and condensed mass are measured independently in a statistically significant sample of cirrus layers. Because such a database is not yet available, we utilize the existing published data for this purpose and properly account for the associated uncertainties in the inversion formalism.

The actual retrieval error when the algorithm is applied to data and compared with measurements arises from an accumulation of observational errors, errors in the empirical power-law relationships, and uncertainties in the assumed particle size distribution shape. Although the magnitude of the latter error source is difficult to estimate theoretically, the former two sources of error can be accounted for simultaneously in the covariance matrices of the optimal estimation inversion algorithm [Eq. (15)]. If we assume that a_z, a_m, and a_A have an uncertainty of 100%, that b_z, b_m, and b_A have an uncertainty of 50%, and that the observations Z, β_a, and τ_v have uncertainties of 10%, 40%, and 40%, respectively, and assuming that these uncertainties are uncorrelated, Table 5 summarizes the expected algorithm errors. We find that IWP can be derived to within 40%–50% and particle size to within 50% for the algorithms that use radar reflectivity (ZR and ZS). This is similar but slightly larger than the errors derived using a ground-based version of the ZR algorithm relative to aircraft data (Mace et al. 2005). The uncertainty of the particle size retrieval with the RS algorithm is nearly a factor of 2 and suggests that very little information on particle size can be derived with the RS algorithm. Furthermore, we emphasize that these errors are likely lower limits to the uncertainties because the departures of size distributions from single-mode exponentials will cause additional uncertainty.

3. Evaluation of the algorithms

Data collected during the CRYSTAL FACE mission provide detailed measurements of upper-tropospheric clouds with a set of instruments that mimic the measurements that will be collected from the A-Train. The payload of the NASA ER-2 included MAS, the CPL, and the Cloud Radar System (CRS). The NASA WB-57F aircraft measured in situ microphysical properties with the cloud particle imager (CPI; Lawson and Cormack 1995), the closed-path laser hygrometer total water (CLH; Hallar et al. 2004), and the Harvard Lyman-α Water Vapor Instrument [H2O-V(HU); Weinstock et al. 1994]. We examine two case studies from 26 and 29 July 2002.

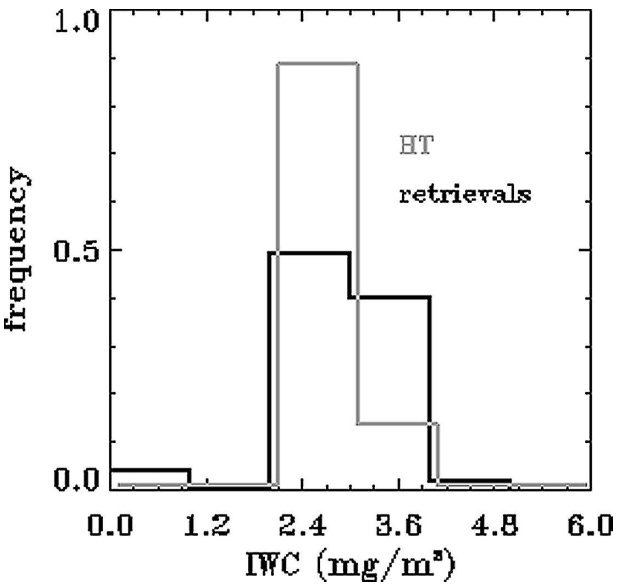

FIG. 14. Histogram of the retrieved layer-mean IWC and in situ measured IWC.

a. *Case 1: 26 July 2002 during the CRYSTAL FACE campaign*

On 26 July 2002 the ER-2 and WB-57F flew southward into the Tropics, eventually paralleling the eastern Yucatan coast, and returned along the same track. We examine a portion of that flight from 1806:00 to 1912:00 UTC. The extensive cirrus field that was observed along this flight track may be representative of much of the tropical cirrus that will be observed by the A-Train. Figure 11a is a three-channel composite visible image, and Fig. 11b is a CO_2 channel image. Both figures show data from MODIS on the *Aqua* satellite, with the aircraft flight tracks plotted on both images. The images show active convection over the Yucatan Peninsula, with cirrus extending offshore to the east and northeast over a field of cumulus. In the CO_2 channel image (channel 34 from MODIS), the lower cumulus clouds are largely obscured by the strong gaseous absorption.

Figure 12 shows the lidar signal, radar reflectivity, MAS brightness temperature T_b in a band similar to the MODIS channel 34, and retrieved layer-mean IWC for the southbound (Fig. 12a) and northbound (Fig. 12b) legs. Much of the cirrus is well below the detection threshold (~ -28 dBZ) of the CRS. In the sections where the CRS observes cirrus, T_b decreases and the lidar backscatter tends to increase. Convection was observed by the CRS on the southbound leg from 1830 to 1836 UTC, and then an anvil was observed at 1850 UTC on the northbound leg that is possibly separated from

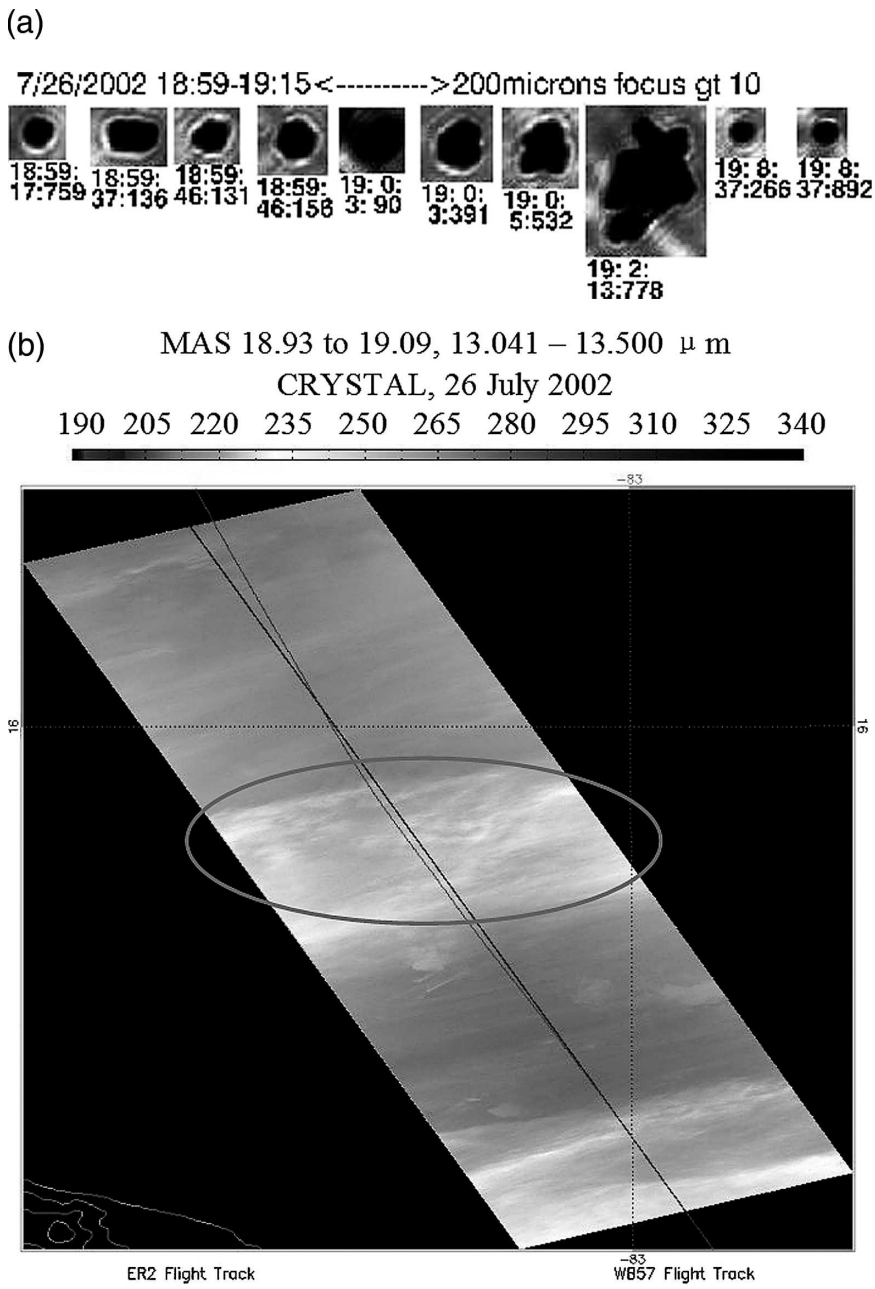

FIG. 15. (a) Particle samples collected by CPI on WB-57F; (b) WB-57F and ER-2 flight tracks overlapped on MAS observation.

the top of the convection observed earlier. Note that T_b decreases in response to these deep clouds—a factor that will need to be accounted for in the operational implementation of the retrieval algorithms. When cirrus occurs above convection or other lower-level optically thick clouds, the emissivity of the cirrus layer is better estimated based on the radar-determined cloud-top temperature.

Cirrus layers often have a vertical structure in which the layer tops are optically tenuous and composed of small particles, with larger particles and higher water contents in the lower portions of the layer (Mace et al. 1997). Cloud radars are known often to not sense the full vertical extent of cirrus layers because of this characteristic structure (Sassen and Mace 2002). We find such a structure in the tropical cirrus observed on 26 July. Because the ZR algorithm requires the layer-averaged value of Z (i.e.,

$$\overline{Z} = \frac{\sum_{\text{base}}^{\text{top}} Z(h)}{\Delta h},$$

where h denotes height and Δh denotes layer thicknesses), using the radar to estimate Δh would often result in systematic biases in the derived cloud properties with the ZR algorithm. Because

$$\sum_{\text{base}}^{\text{top}} Z(h)$$

is not greatly biased by not sensing the very small values of Z near cloud top, the error arises because of an incorrect value of Δh that results in values of $\overline{Z}$and β_a that are too large. Therefore, when the radar-detected cloud top is lower than the lidar-detected cloud top, the lidar-detected cloud top and the radar-detected cloud base are used to specify the layer thickness in the ZR and ZS algorithms. Specifying the layer thickness in this way will improve retrieval accuracy overall, because the radar reflectivity factors below the sensitivity of the radar do not contribute much to

$$\sum_{\text{base}}^{\text{top}} Z(h).$$

The three algorithms tend to be consistent with one another when this procedure is employed.

In the 26 July case, the WB-57F penetrated the cloud layer at around 1900 UTC, and the aircraft flight track is illustrated together with the ER-2 observations in Fig. 13. The layer-mean IWC retrieved from the RS algorithm is plotted together with in situ measurements in Fig. 13d. After 1900 UTC, the Harvard IWC data (Weinstock et al. 1994) fall within our 1-standard-deviation (sigma) uncertainty of the retrieval. Figure 14 shows the histogram of the retrieved layer-mean IWC and in situ measured IWC. The retrieved IWC is much larger than the in situ data before 1900 UTC because the WB-57F only flew through the upper portion of the layer and most of the condensed mass is concentrated near cloud base where the CRS is able to sense the cloud; recall that we are retrieving the layer-mean IWC with these algorithms. The overlap of the ER-2 and WB-57F flight tracks is depicted in Fig. 15b. The larger layer-mean IWC is also evident by the decrease in MAS brightness temperature and is indicated by the circled area in Fig. 15b. Figure 15a is the particle sample collected by the CPI (data supplied by A. Heymsfield 2004, personal communication) on the WB-57 and shows small, quasi-spherical ice crystals. For these ice crystals, b_m is close to 3 and b_A is close to 2.

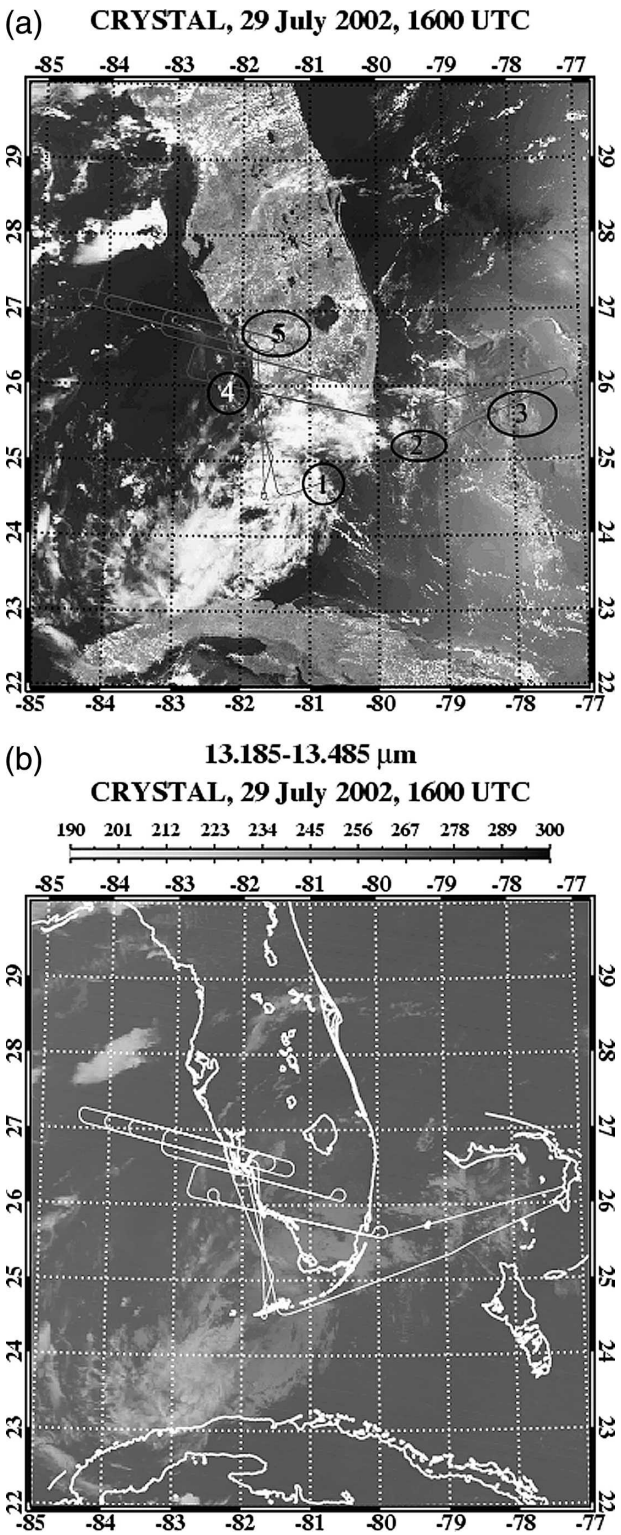

FIG. 16. (a) The visible-channel observations from MODIS on *Aqua* on 29 Jul 2002 with the ER-2 aircraft flight track in gray. Circle 1 shows the thick cirrus at around 1551 UTC, circle 2 shows the thin cirrus at around 1603 UTC, circle 3 shows the thick cirrus at around 1618 and 1636 UTC, circle 4 shows the thick cirrus at around 1706 UTC, and circle 5 shows the anvil at around 1845 UTC. (b) The CO_2-channel observations from MODIS on *Aqua* on 29 Jul 2002, with the ER-2 aircraft flight track in white.

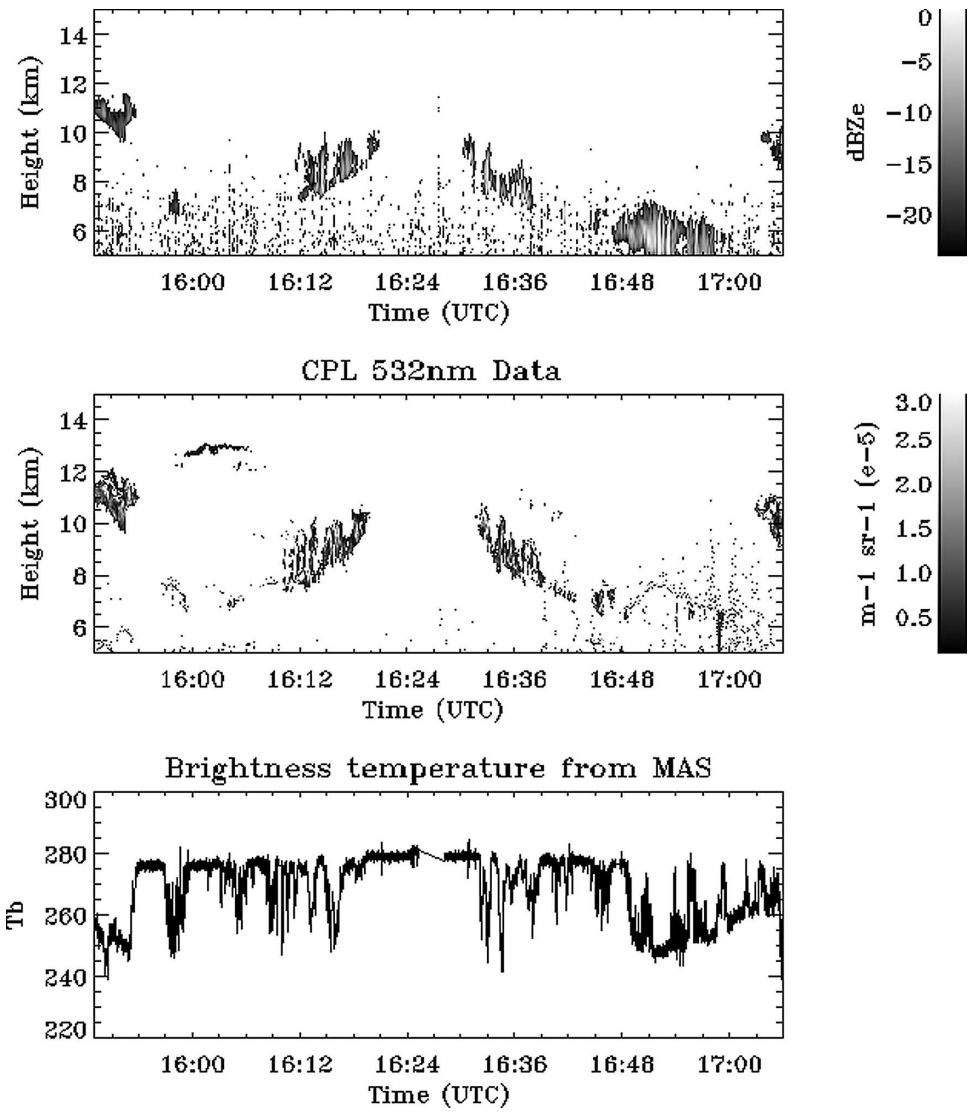

FIG. 17. ER-2 observations on 29 Jul 2002: radar reflectivity from CRS, normalized lidar signal from CPL, and brightness temperature from MAS.

b. Case 2: 29 July 2002 during the CRYSTAL FACE campaign

On 29 July 2002, there was cirrus off the east coast of Florida in the early afternoon, and a significant thunderstorm developed north of Naples around 1730 UTC that produced an extensive cloud deck moving northwestward off the Florida coast later in the day. The ER-2 flew a north–south traverse along Florida's west coast and then back to Key West over the water. The ER-2 then headed off the east coast of Florida and over the Bahamas. Several legs were then flown across the east and west ground sites near Miami International Airport and Everglades City, Florida, respectively. Following the legs over the ground sites, east–west legs north of the ground sites were conducted over the thunderstorm anvils in the Naples area. Similar to Fig. 11, Figs. 16a and 16b show the MODIS visible composite image and CO_2 channel images from *Aqua* with the ER-2 flight track overlaid.

Figure 17 shows the three observations from the ER-2 aircraft for the time period from 1548 to 1706 UTC, and results from the retrieval algorithms are depicted in Fig. 18. The cirrus properties are variable during this period. The properties of the thick cirrus are retrieved from the two radar-dependent algorithms, and those of the thin cirrus occurring around 1603:00 UTC, which are below the detection threshold of the

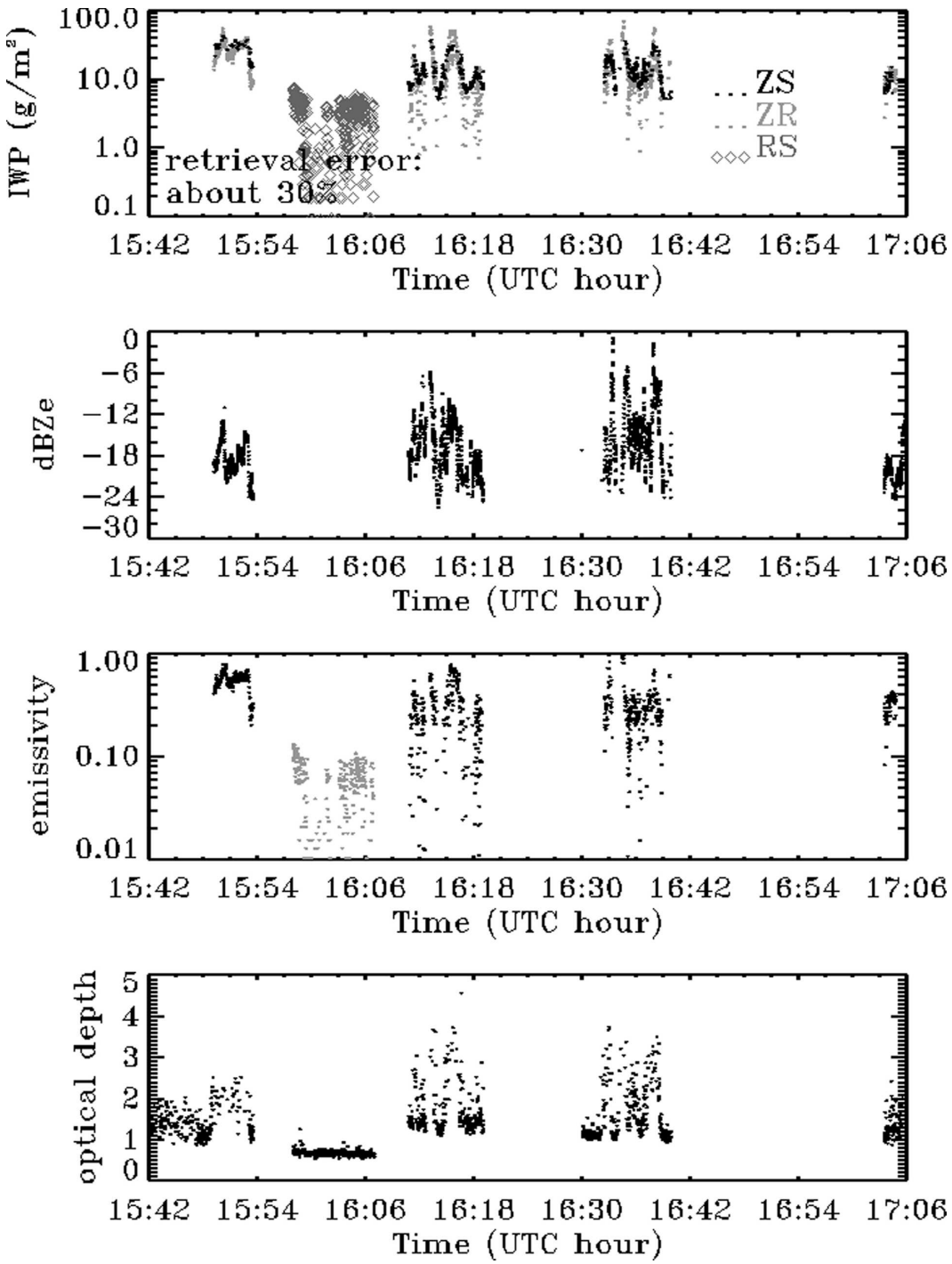

FIG. 18. A time series of retrieved IWP, layer-averaged radar reflectivity, cloud-layer emissivity derived from MAS observations, and optical depth.

CRS, are retrieved from the RS algorithm. The two radar-dependent retrievals agree well for cirrus during the period from 1548 to 1554 UTC but demonstrate some scatter for the other two thick cirrus periods around 1618 and 1633 UTC. The retrievals from the ZR algorithm vary with time because of the variability in the cloud-layer emittances. A high correlation (0.8) with an rms of 5 is found between the IWPs retrieved from the ZS and the ZR algorithms for the whole time period.

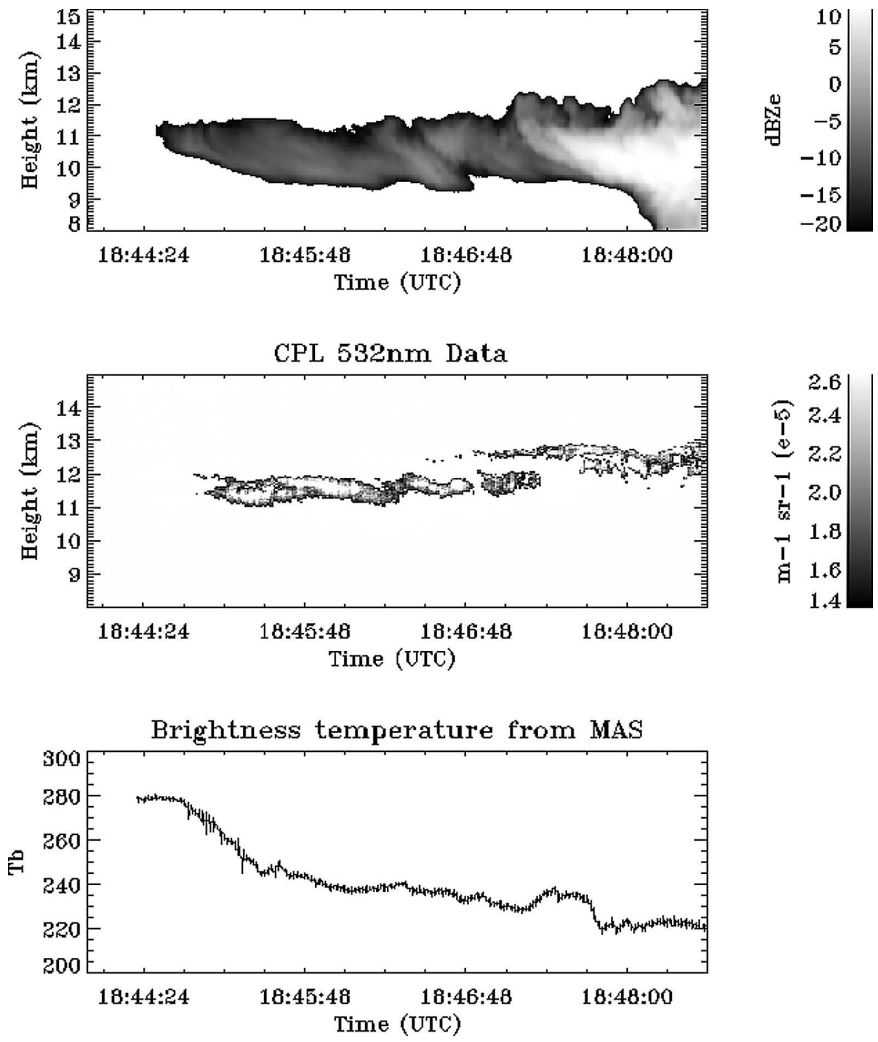

FIG. 19. ER-2 observations for the convection and the anvil on 29 Jul 2002 from CRS, CPL, and MAS.

Later during the 29 July flight, the ER-2 sampled the aging thunderstorm anvil as it advected over the Gulf of Mexico west of Naples. In Figs. 19 and 20 we show the ice water path derived using the ZR algorithm (the lidar signal was attenuated along most of this track). We find that the IWP increases steadily from near 30 g m^{-2} near the western extent of the anvil until the cloud becomes optically thick and the emissivity approaches 1 at an IWP of approximately 110 g m^{-2}.

c. Ground-based evaluation

In situ data can provide reliable information about actual cloud properties, but such data are not routinely available. Therefore, to characterize the algorithms in a statistical sense, we turn to the routine ground-based measurements at the ARM SGP site. As a reference algorithm we use the ground-based radar-reflectivity- and interferometer-based approach (Mace et al. 2005) that has been developed and applied extensively to ARM observations (Mace et al. 2001, 2005). This algorithm, hereinafter referred to as the A-ZR algorithm, has been validated using aircraft data and now has reasonably well known error characteristics, as discussed in Mace et al. (2005), where it is shown that the uncertainty in the layer-mean effective radius r_e and IWP are on the order of 30% and 20%, respectively, with negligible bias. The A-ZR algorithm is theoretically similar to the ZR algorithm in that both use layer-mean radar reflectivity and estimates of emissivity. However, the differences in the methodological approaches are substantial, and comparing the two algorithms does provide relevant information as to the validity of the method used in the ZR algorithm.

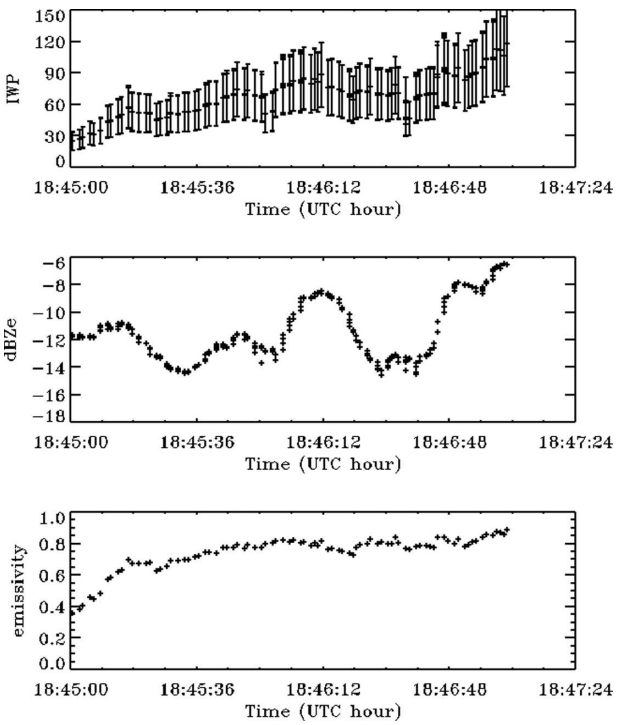

FIG. 20. Retrieved IWP of the anvil with estimated errors, layer-averaged radar reflectivity, and cloud-layer emissivity.

Our approach is to use the ground-based MMCR and MPL data collected at the ARM site combined with MODIS-derived layer emissivity values as input to the algorithm ZR and RS algorithms. The ZS algorithm will use just the ground-based radar and lidar data as input. Combining ground-based active remote sensor data with emissivity values derived from space can be a difficult undertaking. Using the approach described in Mace et al. (2005), where MODIS cloud property retrievals were compared with ground-based retrievals with the A-ZR algorithm, a 15 km $\times$ 15 km region (centered on the ARM SGP site) from the MODIS granule is selected, and the pixels (with 1-km resolution) in this region are considered. Because the typical wind velocity at cirrus levels is about 25 m s^{-1}, the radar reflectivity factor and the lidar-derived transmissivity are averaged for 10 min to combine with MODIS data for retrieving cirrus microphysical properties.

The results are shown in Figs. 21a–c derived from the MODIS overpasses of the SGP site listed in Table 6. The retrieval means and their standard deviations are plotted together in Fig. 21 and are summarized in Table 7. The correlation coefficients are similar for the three algorithms, and are larger than 0.9. The slope for the linear regression for the ZR algorithm is slightly larger than 1, and those for the ZS and RS algorithms are slightly smaller than 1. The bias is relatively small, and the differences come from the fact that the effective density (Brown and Francis 1995) in the A-ZR algorithm is a different treatment than the empirical constants used in the algorithms described here. The comparisons show good overall agreement, however.

Because the ZS algorithm does not rely on space-based measurements and the results for the ZS algorithm are in reasonable agreement with the ZR and RS algorithms, we assume that any added uncertainty resulting from combining the ground-based and space-based measurements would show up as additional scatter in the ZR and RS comparisons beyond what the ZS algorithm comparison shows. The comparison results (Table 7) are, in fact, actually identical in the correlation coefficient and have similar magnitudes in the regression slope and bias. We do see an increase in the bias standard deviation, suggesting an increase in the scatter about the linear regression line. This increase in scatter is possibly due to combining the ground-based measurements with the space-based measurements. The difference in sign of the mean bias of the ZS algorithm comparison is interesting but it is impossible to determine if it is due to the algorithms themselves or to the MODIS data being combined quantitatively with ground-based measurements.

4. Summary

A suite of algorithms, referred to as the ZR, ZS, and RS algorithms, for retrieving cirrus IWP and layer-mean mass-mean particle size from multiple remote sensors has been developed for airborne and spaceborne millimeter radar, optical lidar, and infrared radiometer measurements. The algorithms exploit the synergy of the active and passive measurements to treat a wide range of cirrus situations, ranging from optically tenuous cirrus in the tropopause transition layer in the Tropics to thicker cirrus that populate up to 30% of the global troposphere. Operational implementation of these algorithms to A-Train data will provide the opportunity to extend significantly our present understanding of the global distribution of cirrus cloud properties.

The algorithms involve consideration of the properties of ice crystals and make use of empirical power-law relations between the maximum dimension of ice crystals and their cross-sectional area, radar backscatter cross section, and mass. By assuming an exponential size distribution, cloud-layer-mean IWP and mass-mean particle size (L_{mass}) are retrieved from the observations. The system of forward-model equations is solved using an optimal estimation framework that converges to a solution with high efficiency and also provides quantitative uncertainties of the retrieved values.

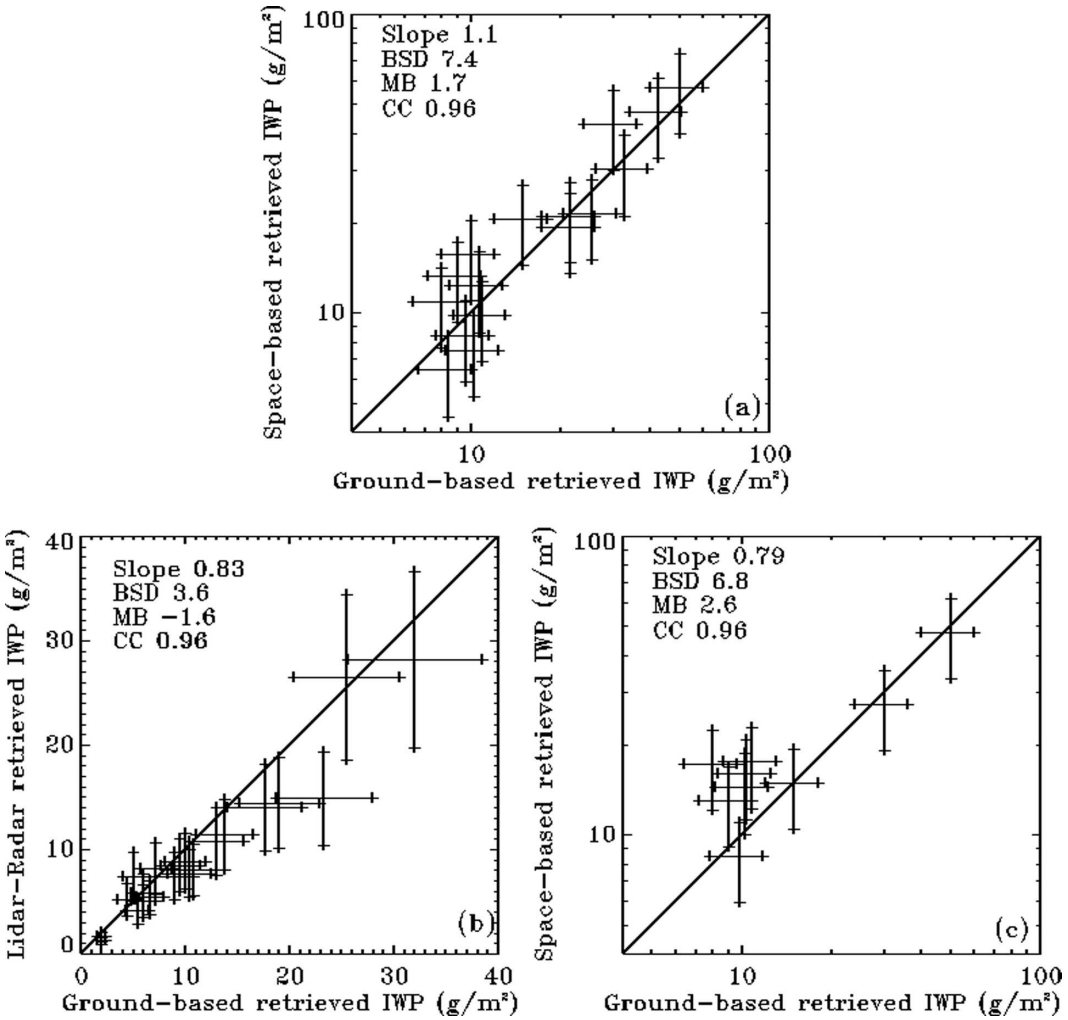

FIG. 21. (a) Comparison between the ground-based retrieval and the ZR algorithm. (b) Comparison between the ground-based retrieval and the ZS algorithm. (c) Comparison between the ground-based retrieval and the RS algorithm.

The sensitivity of the two radar-dependent algorithms to the input data reveals that retrieved IWPs depend to a nearly equal degree on the two input observations, whereas retrieved particle sizes are more sensitive to radar reflectivity. The RS algorithm is the most unstable among the three because of the second-moment dependence of both observations. The retrieved quantities are sensitive to errors in the observations and to uncertainties in the empirical constants describing the relationships between the ice crystal maximum dimension and the ice crystal area and mass assumed in the algorithms. When the most likely uncertainties in the inputs and parameters are taken into account, we find that the condensed mass can be retrieved to within 40%–50% and that the mass-mean particle size can be retrieved to within 50% for the algorithms that rely on radar. The particle size uncertainty for the algorithm derived for lidar optical depth and infrared emissivity is nearly a factor of 2 and suggests that this algorithm has minimal skill in retrieving particle size, although the mass retrieval uncertainty is approximately 50%. These errors represent a lower bound because they do not account for uncertainties associated with the particle size distribution shape.

The suite of algorithms is implemented using data collected during the CRYSTAL FACE mission in July 2002 when the NASA ER-2 payload included the CRS, CPL, and MAS. Two case studies show the necessity of multiple remote sensors and algorithms to cover the wide dynamic range of cirrus properties. In comparing the retrieved layer-averaged IWC with data collected by water content probes on the WB-57F, it is seen that the RS algorithm produces reasonable values with in situ measurements falling within 1 sigma of uncertainty

TABLE 6. Date, overpass time, and viewing angle for the cases used for the validation of the suite of algorithms.

Date	Overpass time (UTC)	Viewing angle (°)
27 Nov 2000	1707:14	47.8
28 Nov 2000	1749:55	24.1
30 Nov 2000	1737:39	1
22 Mar 2001	1735:27	2.5
27 May 2001	1722:08	21.4
6 Jun 2001	1758:21	42.2
3 Sep 2001	1750:03	34.4
4 Sep 2001	1654:58	53.3
25 Nov 2001	1640:07	62.7
	1817:45	63.1
21 Dec 2001	0513:53	52.9
	1715:43	22.1
16 Mar 2002	0352:51	59.3
30 Mar 2002	0405:13	49
	1744:41	33.7
15 Jun 2002	0512:25	53.3
20 Jul 2002	0405:21	48.7
9 Nov 2002	0404:41	49.2
29 Nov 2002	0518:13	58.4
	1720:04	10.4
16 Dec 2002	0423:24	24.4
	18:02:52	54.4
17 Dec 2002	0506:06	47.5
	1708:03	31.6

estimated from algorithm errors. The three algorithms are consistent within the estimated uncertainties for the first case study, and there is a high correlation (0.8) between the two radar-dependent algorithms for the second study. The three algorithms are evaluated with the A-ZR algorithm separately, and a good linear relationship between the validated A-ZR algorithm and the suite of the algorithms is found, with correlation coefficients around 0.96. There are also reasonably small bias and standard deviations for the comparisons (Table 7).

The algorithms are expected to facilitate the analysis of the extensive high-cloud dataset from the A-Train data streams. We anticipate implementing the algorithms on an experimental basis as the A-Train data become available. Current results are satisfactory, but more work is needed in terms of validation and implementation. The algorithms are presently not valid in situations in which deep lower-level clouds extend into the middle troposphere and influence the 13-μm radiance. Multiple cirrus layers are also not accounted for in the current version of the algorithms. Because the empirical constants that relate mass and area to particle maximum dimension are critical to the algorithm accuracy and our goal is to process global data, it is clear that more in situ data are needed to constrain these empirical relationships. Validation will continue as more field experiment data become available.

TABLE 7. The correlation coefficient (CC), mean bias (MB), bias standard deviation (BSD), and slope for the three algorithms compared with the A-ZR algorithm.

Algorithm	Slope	BSD	MB	CC
ZR	1.1	7.4	1.7	0.96
ZS	0.83	3.6	−1.6	0.96
RS	0.79	6.8	2.6	0.96

Acknowledgments. We acknowledge the assistance of Dr. Ping Yang of Texas A&M University who provided the infrared optical properties. This work would not have been possible without his assistance. This research has been supported primarily through the NASA Radiation Science Program (NNG04GL92G and NNG04GG82G). Aircraft data were kindly provided by G. M. Heymsfield (CRS) and M. McGill (CPL) from the NASA Goddard Space Flight Center, and E. Weinstock from Harvard University. CPI imagery was provided by A. Heymsfield. The ground-based observational data were obtained from the Atmospheric Radiation Measurement Program sponsored by the U.S. Department of Energy, Office of Science, Office of Biological and Environmental Research, Environmental Science Division. We thank Sally Benson for help on the IDL program and data reduction.

REFERENCES

Ackerman, T. P., and G. M. Stokes, 2003: The Atmospheric Radiation Measurement Program. *Phys. Today,* **56,** 38–44.

——, K. N. Liou, F. P. J. Valero, and L. Pfister, 1988: Heating rates in tropical anvils. *J. Atmos. Sci.,* **45,** 1940–1948.

Aydin, K., and T. M. Walsh, 1999: Millimeter wave scattering from spatial and planar bullet rosettes. *IEEE Trans. Geosci. Remote Sens.,* **37,** 1138–1150.

Benedetti, A., G. L. Stephens, and J. M. Haynes, 2003: Ice cloud microphysics retrievals from millimeter radar and visible optical depth using an estimation theory approach. *J. Geophys. Res.,* **108,** 4335, doi:10.1029/2002JD002693.

Brown, P. R. A., and P. N. Francis, 1995: Improved measurements of the ice water content in cirrus using a total water probe. *J. Atmos. Oceanic Technol.,* **12,** 410–414.

Cess, R. D., and Coauthors, 1996: Cloud feedback in atmospheric general circulation models: An update. *J. Geophys. Res.,* **101,** 12 791–12 794.

Comstock, J. M., T. P. Ackerman, and G. G. Mace, 2002: Ground-based lidar and radar remote sensing of tropical cirrus clouds at Nauru Island: Cloud statistics and radiative impacts. *J. Geophys. Res.,* **107,** 4714, doi:10.1029/2002JD002203.

Cooper, S. J., T. S. L'Ecuyer, and G. L. Stephens, 2003: The impact of explicit cloud boundary information on ice cloud microphysical property retrievals from infrared radiances. *J. Geophys. Res.,* **108,** 4107, doi:10.1029/2002JD002611.

Del Genio, A. D., M.-S. Yao, W. Kovari, and K.-W. Lo, 1996: A

prognostic cloud water parameterization for global climate models. *J. Climate,* **9,** 270–304.

Doviak, R. J., and D. S. Zrnic, 1993: *Doppler Radar and Weather Observations*. 2d ed. Academic Press, 562 pp.

Dowling, D. R., and L. F. Radke, 1990: A summary of the physical properties of cirrus clouds. *J. Appl. Meteor.,* **29,** 970–978.

Fu, R., A. D. Del Genio, and W. B. Rossow, 1990: Behavior of deep convective clouds in the tropical Pacific deduced from ISCCP radiances. *J. Climate,* **3,** 1129–1152.

Hallar, A. G., L. M. Avallone, R. L. Herman, B. E. Anderson, and A. J. Heymsfield, 2004: Measurements of ice water content in tropopause region arctic cirrus during the SAGE III Ozone Loss and Validation Experiment (SOLVE). *J. Geophys. Res.,* **109,** D17203, doi:10.1029/2003JD004348.

Heymsfield, A. J., 2003: Properties of tropical and midlatitude ice cloud particle ensembles. Part I: Median mass diameters and terminal velocities. *J. Atmos. Sci.,* **60,** 2573–2593.

——, and J. Iaquinta, 2000: Cirrus crystal terminal velocities. *J. Atmos. Sci.,* **57,** 916–942.

——, and Coauthors, 2002: Observations and parameterizations of particle size distributions in deep tropical cirrus and stratiform precipitating clouds: Results from in situ observations in TRMM field campaigns. *J. Atmos. Sci.,* **59,** 3457–3491.

——, C. G. Schmitt, A. Bansemer, D. Baumgardner, E. M. Weinstock, J. T. Smith, and D. Sayres, 2004: Effective ice particle densities for cold anvil cirrus. *Geophys. Res. Lett.,* **31**, L02101, doi:10.1029/2003GL018311.

Jensen, E., D. Starr, and O. B. Toon, 2004: Mission investigates tropical cirrus clouds. *Eos, Trans. Amer. Geophys. Union,* **85,** 45–50.

King, M. D., S. Platnick, P. Yang, G. T. Arnold, M. A. Gray, J. C. Riedi, S. A. Ackerman, and K. Liou, 2004: Remote sensing of liquid water and ice cloud optical thickness and effective radius in the Arctic: Application of airborne multispectral MAS data. *J. Atmos. Oceanic Technol.,* **21,** 857–875.

Lawson, R. P., and R. H. Cormack, 1995: Theoretical design and preliminary tests of two new particle spectrometers for cloud microphysics research. *Atmos. Res.,* **35,** 315–348.

Li, L., G. M. Heymsfield, P. E. Racette, L. Tian, and E. Zenker, 2004: A 94-GHz cloud radar system on a NASA high-altitude ER-2 aircraft. *J. Atmos. Oceanic Technol.,* **21,** 1378–1388.

Liao, X., W. B. Rossow, and D. Rind, 1995: Comparison between SAGE II and ISCCP high-level clouds. 1: Global and zonal mean cloud amounts. *J. Geophys. Res.,* **100,** 1121–1135.

Liou, K. N., 1986: Influence of cirrus clouds on weather and climate processes: A global perspective. *Mon. Wea. Rev.,* **114,** 1167–1199.

——, 2002: *An Introduction to Atmospheric Radiation*. Academic Press, 583 pp.

Liu, C.-L., and A. J. Illingworth, 2000: Toward more accurate retrievals of ice water content from radar measurement of clouds. *J. Appl. Meteor.,* **39,** 1130–1146.

Mace, G. G., T. P. Ackerman, and E. E. Clothiaux, 1997: A study of composite cirrus morphology using data from a 94-GHz radar and correlations with temperature and large-scale vertical motion. *J. Geophys. Res.,* **102** (D12), 13 581–13 593.

——, E. E. Clothiaux, and T. A. Ackerman, 2001: The composite characteristics of cirrus clouds: Bulk properties revealed by one year of continuous cloud radar data. *J. Climate,* **14,** 2185–2203.

——, A. J. Heymsfield, and M. R. Poellot, 2002: On retrieving the microphysical properties of cirrus clouds using the moments of the millimeter-wavelength Doppler spectrum. *J. Geophys. Res.,* **107,** 4815, doi:10.1029/2001JD001308.

——, Y. Zhang, S. Platnick, M. D. King, P. Minnis, and P. Yang, 2005: Evaluation of cirrus cloud properties derived from MODIS data using cloud properties derived from ground-based observations collected at the ARM SGP site. *J. Appl. Meteor.,* **44,** 221–240.

McGill, M. J., and Coauthors, 2004: Combined lidar-radar remote sensing: Initial results from CRYSTAL-FACE. *J. Geophys. Res.,* **109,** D07203, doi:10.1029/2003JD004030.

Miller, S., G. Stephens, C. Drummond, A. Heidinger, and P. Partain, 2000: A multisensor diagnostic satellite cloud property retrieval scheme. *J. Geophys. Res.,* **105,** 19 955–19 971.

Minnis, P., D. P. Garber, D. F. Young, R. F. Arduini, and Y. Takano, 1998: Parameterizations of reflectance and effective emittance for satellite remote sensing of cloud properties. *J. Atmos. Sci.,* **55,** 3313–3339.

Mitchell, D. L., 1996: Use of mass- and area-dimensional power laws for determining precipitation particle terminal velocities. *J. Atmos. Sci.,* **53,** 1710–1723.

Mitrescu, C., and G. L. Stephens, 2002: A new method for determining cloud transmittance and optical depth using the ARM micropulsed lidar. *J. Atmos. Oceanic Technol.,* **19,** 1073–1081.

Platnick, S., J. Y. Li, M. D. King, H. Gerber, and P. V. Hobbs, 2001: A solar reflectance method for retrieving the optical thickness and droplet size of liquid water clouds over snow and ice surfaces. *J. Geophys. Res.,* **106,** 15 185–15 199.

Platt, C. M. R., and A. C. Dilley, 1981: Remote sounding of high clouds. IV: Observed temperature variations in cirrus optical properties. *J. Atmos. Sci.,* **38,** 1069–1082.

Rodgers, C. D., 2000: *Inverse Methods for Atmospheric Sounding: Theory and Practice*. Series on Atmospheric Oceanic and Planetary Physics, Vol. 2, World Scientific, 256 pp.

Rossow, W. B., and R. A. Schiffer, 1999: Advances in understanding clouds from ISCCP. *Bull. Amer. Meteor. Soc.,* **80,** 2261–2286.

Salomonson, V. V., 1990: The Moderate Resolution Imaging Spectrometer (MODIS). *Proc. of the 28th Aerospace Sciences Meeting,* Reno, NV, AIAA.

——, and D. L. Toll, 1991: Execution phase (C/D) spectral band characteristics of the EOS Moderate Resolution Imaging Spectrometer-Nadir (MODIS-N) facility instrument. *Adv. Space Res.,* **11,** 231–236.

Sassen, K., and G. G. Mace, 2002: Cirrus. *Ground-Based Remote Sensing of Cirrus Clouds,* D. K. Lynch et al., Eds., Oxford University Press, 168–196.

Schneider, T. L., and G. L. Stephens, 1995: Theoretical aspects of modeling backscattering by cirrus ice particles at millimeter wavelengths. *J. Atmos. Sci.,* **52,** 4367–4385.

Stephens, G. L., S.-C. Tsay, J. P. W. Stackhouse, and P. J. Flatau, 1990: The relevance of the microphysical and radiative properties of cirrus clouds to climate and climatic feedback. *J. Atmos. Sci.,* **47,** 1742–1753.

——, and Coauthors, 2002: The Cloudsat Mission and the A-Train. *Bull. Amer. Meteor. Soc.,* **83,** 1771–1790.

Stubenrauch, C. J., W. B. Rossow, F. Chéruy, A. Chédin, and N. A. Scott, 1999: Clouds as seen by satellite sounders (3I) and imagers (ISCCP). Part I: Evaluation of cloud parameters. *J. Climate,* **12,** 2189–2213.

Wang, P. H., P. Minnis, M. P. McCormick, G. S. Kent, and K. M. Skeens, 1996: A 6-year climatology of cloud occurrence frequency from stratospheric aerosol and Gas Experiment II observations (1985-1990). *J. Geophys. Res.,* **101,** 407–429.

Warren, S. G., 1984: Optical constants of ice from the ultraviolet to the microwave. *Appl. Opt.,* **23,** 1206–1225.

Weinstock, E. M., and Coauthors, 1994: New fast response photofragment fluorescence hygrometer for use on the NASA ER-2 and the Perseus remotely piloted aircraft. *Rev. Sci. Instrum.,* **65,** 3544–3554.

Wylie, D. P., and W. P. Menzel, 1989: Two years of cloud cover statistics using VAS. *J. Climate,* **2,** 380–392.

——, and ——, 1999: Eight years of high cloud statistics using HIRS. *J. Climate,* **12,** 170–184.

——, ——, H. M. Woolf, and K. I. Strabala, 1994: Four years of global cirrus cloud statistics using HIRS. *J. Climate,* **7,** 1972–1986.

Yang, P., and Coauthors, 2004: Spectral signature of cirrus clouds in the far-infrared region: Single-scattering calculation and radiative sensitivity study. *J. Geophys. Res.,* **108,** 4569, doi:10.1029/2002JD003291.

Young, S. A., 1995: Analysis of lidar backscatter profiles in optically thin clouds. *Appl. Opt.,* **34,** 7019–7031.